UNIVERSITY OF LEEDS

This is a repository copy of *High-resolution central-upwind scheme for second-order macroscopic traffic flow models*.

White Rose Research Online URL for this paper:
https://eprints.whiterose.ac.uk/165593/

Version: Accepted Version

Article:
Chen, J, Liu, R orcid.org/0000-0003-0627-3184 and Hu, Y (2020) High-resolution central-upwind scheme for second-order macroscopic traffic flow models. International Journal of Modern Physics C, 31 (07). 2050097. ISSN 0129-1831

https://doi.org/10.1142/s0129183120500977

This is an author produced version of an article published in International Journal of Modern Physics C. Uploaded in accordance with the publisher's self-archiving policy.

Reuse
Items deposited in White Rose Research Online are protected by copyright, with all rights reserved unless indicated otherwise. They may be downloaded and/or printed for private study, or other acts as permitted by national copyright laws. The publisher or other rights holders may allow further reproduction and re-use of the full text version. This is indicated by the licence information on the White Rose Research Online record for the item.

Takedown
If you consider content in White Rose Research Online to be in breach of UK law, please notify us by emailing eprints@whiterose.ac.uk including the URL of the record and the reason for the withdrawal request.

White Rose university consortium
Universities of Leeds, Sheffield & York

eprints@whiterose.ac.uk
https://eprints.whiterose.ac.uk/

Please cite the paper as:
Chen, J., Liu, R. and Hu, Y. (2020) High-resolution central-upwind scheme for second-order macroscopic traffic flow models. International Journal of Modern Physics C, 31(7), 2050097.
DOI: 10.1142/S0129183120500977.

High-resolution central-upwind scheme for second-order macroscopic traffic flow models

Jianzhong Chen[a] , Ronghui Liu[b] and Yanmei Hu[a]

[a]*College of Automation, Northwestern Polytechnical University, Xi'an 710072, China*
[b]*Institute for Transport Studies, University of Leeds, Leeds LS2 9JT, UK*

ABSTRACT
Traffic flow models are important tools for traffic management applications such as traffic incident detection and traffic control. In this paper, we propose a novel numerical approximation method for second-order macroscopic traffic flow models. The method is based on the semi-discrete central-upwind numerical flux and high-order reconstructions for spatial discretizations. We then apply the designed high-resolution schemes to three representative types of second-order traffic flow models and perform a variety of numerical experiments to validate the proposed methods. The simulation results illustrate the effectiveness, simplicity and universality of the central-upwind scheme as numerical approximation method for macroscopic traffic flow models.
Keywords: Traffic flow model; Central-upwind scheme; Numerical approximation; High-resolution

1. Introduction

Traffic congestion is a worldwide growing problem. It has serious impact on the economy, safety and environment. Therefore, how to eliminate the negative effects of traffic congestion has attracted considerable attention. Researchers so far have proposed a variety of models, which are usually classified as microscopic models, mesoscopic models and macroscopic models in terms of the detailed traffic characteristics represented. Among them, macroscopic traffic flow models focusing on the collective behaviour of vehicles are a popular strand of models, and most of them follow the hyperbolic conservation law form [1-10]. A key feature of this type formulation is that it allows both smooth and discontinuous solutions. An example of discontinuous solutions in traffic flow theory is shock waves [1].

The kinematic wave model of Lighthill and Whitham [2], and Richards [3] (LWR

model) is the first macroscopic model of traffic flow. The model employs fluid dynamic principle to represent traffic flow on long crowded roads and is shown to successfully represent the shock-waves on the highways. A discretization of the LWR model employing the first-order Godunov scheme [11,12] leads to a widely applied discrete macroscopic model, namely the cell transmission model (CTM) [13,14]. The LWR model has certain deficiencies, for example in its representations of heterogeneity in driver behaviour, shock structure, and traffic instability (see [4] for details). There are two important extensions of LWR model. The first extension develops second-order models which contain the acceleration equation in addition to the continuity equation. The Payne-Whitham (PW) type models [5-7] were firstly proposed and investigated. After the critique of the PW model for its isotropic nature [15], Aw and Rascle (AR) type models [8,9] were gradually developed. Treiber et al. [16,17] proposed the gas-kinetic-based traffic model (GKT model) which is a second-order nonlocal macroscopic traffic flow model. A more detailed discussion of second-order traffic flow models can be found in [17]. The second extension considers heterogeneous traffic and develops multi-class models; examples can be found in [10,18].

The second-order macroscopic traffic flow models cannot be solved by analytical method for general initial/boundary value problems. It is necessary to introduce numerical methods to obtain approximate solutions. The widely used numerical approximation methods are the finite difference method and the finite volume method. Lower order numerical methods have been applied to solve the second-order models. Zhang [19] developed a finite difference scheme for the PW model [5,6] and Zhang model [7] based on an extension of Godunov scheme [11]. Morgan [20] employed the Lax-Friedrichs scheme and Roe's upwind scheme to approximate some second-order traffic flow models such as the PW model [5,6] and the AR model [8]. Jin and Zhang [21] extended the first-order Godunov scheme to solve the homogeneous part of the PW model. In [22], Godunov-type schemes are developed for the LWR model, the PW model and the Zhang model [7]. Niyitegeka [23] discussed the Riemann problem of the LWR model and the AR model [8], and applied Godunov scheme [11] to solve these models.

However, some of lower order schemes such as the Lax-Friedrichs scheme may

produce a smeared resolution of discontinuities due to excessive numerical dissipation. For example, Zhang et al. [24] studied the multi-class LWR (MC-LWR) model, and the numerical results showed that the lower order scheme might miss catching some very important features of the solution, such as the shocks. Moreover, the resolution of the Lax-Friedrichs scheme using 6400 grid points is similar to that of the fifth weighted essentially non-oscillatory (WENO) [25] using 100 grid points. Some schemes such as Godunov-type upwind schemes with exact or approximate Riemann solvers may require developing different solvers for different models [22,26,27]. The computation of Riemann solvers and related characteristic decompositions is very intricate and time-consuming.

The primary motivation of this study is to design and provide a universal numerical discretization framework for approximating second-order traffic flow models. In this framework, the method can be applicable to different types of second-order models and moreover the method can be easily implemented to new developed macroscopic models, for example, the model describing semi-automated vehicles [28,29] and automated vehicles. Furthermore, the method is able to resolve the problems in which solutions contain rich region structures and can capture the structure of all waves, which may be completely obscured by the excessive numerical dissipation of lower order schemes. In addition, the method does not involve the costly exact or approximate Riemann solvers, which is necessary for Godunov-type upwind schemes. For Godunov-type upwind schemes, different solvers are also needed to be constructed for different macroscopic traffic flow models [22,26,27]. The second goal of this paper is to validate and demonstrate the advantages of high-order numerical discretization methods over lower order methods for traffic flow models by comparing the performance on different second-order macroscopic models.

The WENO scheme [25] and high-order relaxation scheme have been applied to solving the MC-LWR models with heterogeneous drivers [24,30] and on an inhomogeneous highway [10,31], respectively. Using high-resolution relaxation schemes to approximate the solutions of second-order traffic flow models was presented in [29,32]. The relaxation scheme is based on constructing a linear system with stiff relaxation source term (known as the relaxation system) to replace the given conservation law. However, the

relaxation system is larger than the original system, and moreover, the implicit-explicit Runge-Kutta method is used for the time discretization of relaxation scheme. As such, the relaxation scheme is relatively expensive in computational cost.

In this work, we focus on a different type of high-resolution finite volume scheme, the so-called central-upwind (CU) scheme originally introduced by Kurganov et al. [33], which admits a particularly simple semi-discrete form. The CU schemes have been widely studied in the field of computational fluid dynamics. The construction of the CU schemes includes three steps: reconstruction, evolution and projection. In derivation of the CU schemes, the integration over nonuniform control volumes that contain the entire Riemann fans still belongs to the central schemes framework. Thus, they retain the simplicity of the central schemes, namely they do not require Riemann solvers and characteristic decomposition. At the same time, the local speeds of propagation are utilized to define such control volumes. This feature makes the schemes to have a certain upwind nature. The CU schemes have been extended to cluster dynamics equations [34], shallow water systems [35-37] and so on. The CU scheme for a two-class LWR traffic flow model and the MC-LWR model with heterogeneous drivers were presented in [38,39]. Kurganov and Polizzi [40] implemented the second-order non-oscillatory central scheme of Nessyahu and Tadmor [41] and the CU scheme to solve a traffic flow model with Arrhenius look-ahead dynamics. In [42], the LWR model with non-local velocity was investigated, and the second-order central scheme [41] were employed to solve the model. As far as we are aware, there are very few studies implementing the CU scheme for second-order traffic flow models.

The contributions of this paper are threefold. First, a simple and Riemann-solver-free approximation method is introduced to obtain numerical solutions of traffic flow models. Second, high-order reconstructions are implemented to achieve high-order numerical discretization schemes. The superiority of the high-order discretization schemes over low order methods are validated on various numerical simulations of three representative types of second-order models. Third, the present numerical discretization procedures can be used for approximating different second-order traffic flow models using the same framework.

This paper is organized as follows. In Section 2, we give a brief review of second-order macroscopic traffic flow models. In section 3, we describe the procedures of numerical discretization. The numerical tests are shown in section 4. The conclusions are presented in section 5.

2. Second-order traffic flow models

The basic equation of the LWR model is:

$$\rho_t + (\rho v)_x = 0, \tag{1}$$

where ρ and v are the traffic density and speed, respectively. In model (1), the speed is determined by an equilibrium speed-density relationship

$$v = v_e(\rho). \tag{2}$$

As an important extension of the LWR model, the second-order macroscopic models take acceleration into account, and replace Eq. (2) with a momentum equation. We here consider the following three types second-order models.

2.1. The PW type models

Payne [5] and Witham [6] independently proposed the first second-order model, the so called PW model. The momentum equation is given by

$$v_t + vv_x + \frac{1}{\rho} p(\rho)_x = \frac{v_e(\rho) - v}{\tau}, \tag{3}$$

where $p(\rho) = c_0^2 \rho$ represents the traffic pressure, with c_0 being the traffic sound speed, and τ is the relaxation time, which is the period of time that the driver adjusts the speed v to the equilibrium speed v_e. For other PW type models, we refer to [7,43,44].

The common features of this type models are that the momentum equation includes the density gradient term, and the model has a characteristic speed greater than the macroscopic speed.

In this type models, we investigate the numerical method for the PW model, which can

be rewritten in the conservative form

$$\begin{cases} \rho_t + q_x = 0, \\ q_t + (q^2/\rho + c_0^2\rho)_x = \dfrac{\rho v_e(\rho) - q}{\tau}, \end{cases} \tag{4}$$

or

$$\mathbf{u}_t + \mathbf{f}(\mathbf{u})_x = \mathbf{s}(\mathbf{u}), \tag{5}$$

where $\mathbf{u} = (\rho, q)^T$ is the state variables (the conserved variables), $q = \rho v$ is the flow, $\mathbf{f}(\mathbf{u}) = (q, q^2/\rho + c_0^2\rho)^T$ is the vector of flux, and $\mathbf{s}(\mathbf{u}) = (0, (\rho v_e(\rho) - q)/\tau)^T$ is the source vector. Based on the computation of the Jacobian matrix $\mathbf{A}(\mathbf{u}) = \partial\mathbf{f}/\partial\mathbf{u}$, the system (5) has the two real and distinct eigenvalues

$$\lambda_{1,2} = v \pm c_0 . \tag{6}$$

Although Del Castillo et al. [45] and Daganzo [15] pointed out several drawbacks of the PW model, we consider this model here because we are mainly concerned with its numerical solution and the performance of the proposed numerical method. We adopt the following equilibrium speed-density relationship used in [4,22,46-49]:

$$v_e(\rho) = 5.0461[(1 + \exp((\rho - 0.25)/0.06))^{-1} - 3.72 \times 10^{-6}]\tilde{l}/\tilde{\tau}, \tag{7}$$

where $\tilde{l}$ and $\tilde{\tau}$ are, respectively, the unit of length and the relaxation coefficient, and ρ is scaled by the jam density $\rho_{\max}$. Figure 1 shows the fundamental diagram of the PW model.

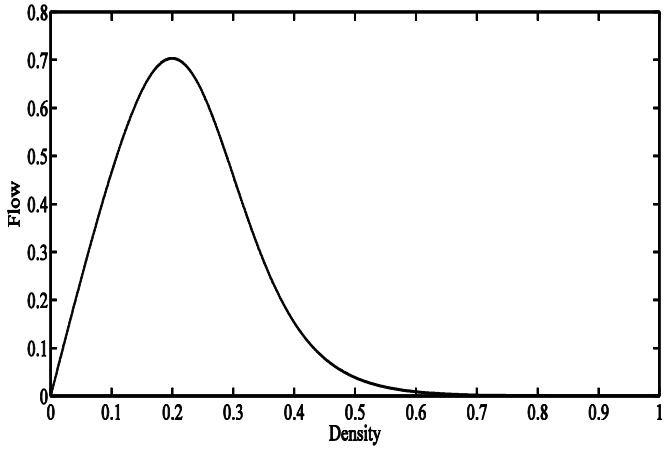

Fig.1. Fundamental diagram of the PW model with $\tilde{l} = 10\,\text{m}$ and $\tilde{\tau} = 10\,\text{s}$.

2.2. The AR type models

To remedy the deficiencies of the PW type models, Aw and Rascle [8] replaced the space derivative of the pressure in Eq. (3) by a convective derivative, and proposed a new macroscopic model, called the AR model. The momentum equation is

$$(v + p(\rho))_t + vv_x + vp(\rho)_x = 0\,, \tag{8}$$

where $p(\rho)$ can have different expressions, but $p(\rho) = \rho^\gamma$ with a parameter $\gamma > 0$ is considered as the prototype. In this work, we use the value $\gamma = 2$.

Zhang [9] developed a similar model, in which the momentum equation is

$$v_t + vv_x + \rho v_e'(\rho) v_x = 0\,. \tag{9}$$

In comparison with the PW type models, the density gradient term in the speed dynamic equation is replaced by the speed gradient term in AR type models, and the characteristic speeds are always less than or equal to the macroscopic flow speed. For other AR type models, we refer to [50–54].

In this type models, we consider the numerical solution for the AR model and the Zhang model, which can be rewritten, respectively, in the conservative form

$$\mathbf{u}_t + \mathbf{f}(\mathbf{u})_x = 0 \quad \text{with} \quad \mathbf{u} = \begin{pmatrix} \rho \\ \rho(v + p(\rho)) \end{pmatrix}, \quad \mathbf{f}(\mathbf{u}) = \begin{pmatrix} \rho v \\ \rho v(v + p(\rho)) \end{pmatrix}, \tag{10}$$

and

$$\mathbf{u}_t + \mathbf{f}(\mathbf{u})_x = 0 \quad \text{with} \quad \mathbf{u} = \begin{pmatrix} \rho \\ y \end{pmatrix}, \quad \mathbf{f}(\mathbf{u}) = \begin{pmatrix} y + \rho v_e(\rho) \\ \frac{y^2}{\rho} + y v_e(\rho) \end{pmatrix}, \tag{11}$$

where $y = \rho v - \rho v_e(\rho)$ is the difference between the actual flow and the equilibrium flow. The eigenvalues of the Jacobian matrix of the model (10) are

$$\lambda_1 = v - \rho p'(\rho)\,, \quad \lambda_2 = v\,. \tag{12}$$

Therefore, the system is strictly hyperbolic, except for $\rho = 0$. The Jacobian matrix of the model (11) has two real and distinct eigenvalues

$$\lambda_1 = v + \rho v_e'(\rho)\,, \quad \lambda_2 = v\,. \tag{13}$$

For the Zhang model, we consider the following equilibrium flow-density relationship

proposed by Mammer et al. [55]:

$$q_e(\rho)=\begin{cases}\rho\left[v_{\max}-\dfrac{\rho}{\rho_{cr}}(v_{\max}-v_{cr})\right], & \text{if } 0\le\rho\le\rho_{cr},\\ w_{\max}(\rho_{\max}-\rho)+\alpha(\rho_{\max}-\rho)^2, & \text{if } \rho_{cr}\le\rho\le\rho_{\max}.\end{cases} \tag{14}$$

Here $v_{\max}$ is the free flow velocity, ρ_{cr} is the critical density, v_{cr} is the critical velocity, $w_{\max}=-q_e'(\rho_{\max})$ and $\alpha=(q_{\max}/(\rho_{\max}-\rho_{cr})^2)-(w_{\max}/(\rho_{\max}-\rho_{cr}))$, where $q_{\max}$ is the maximum flow. Figure 2 shows the fundamental diagram of the Zhang model. In the figure, the parameter values are chosen as:

$$\rho_{\max}=0.2 \text{ veh/m},\ v_{\max}=40 \text{ m/s},\ \rho_{cr}=0.0278 \text{ veh/m},\ v_{cr}=20 \text{ m/s},\ w_{\max}=5 \text{ m/s}. \tag{15}$$

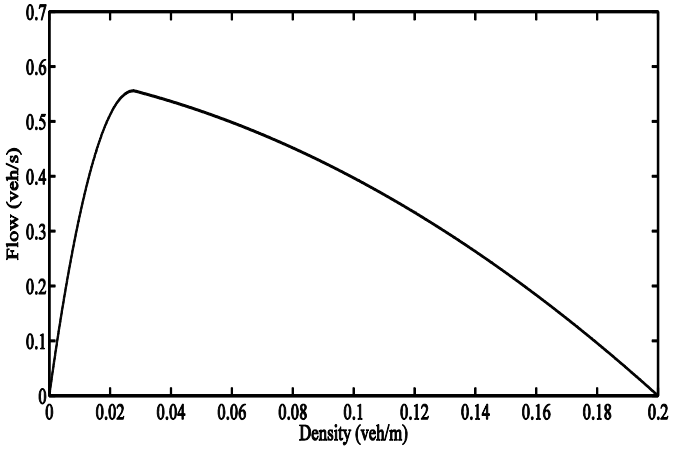

Fig. 2. Fundamental diagram of the Zhang model.

2.3. The GKT model

The GKT model is derived from a microscopic model that explicitly considers vehicle-driver heterogeneities. The GKT model can be written in the conservation form

$$\mathbf{u}_t+\mathbf{f}(\mathbf{u})_x=\mathbf{s}(\mathbf{u}), \tag{16}$$

where $\mathbf{u}=(\rho,q)^T$, $\mathbf{f}(\mathbf{u})=(q,q^2/\rho+p)^T$ and $\mathbf{s}(\mathbf{u})=(0,(\rho v_e-q)/\tau)^T$. The pressure term p is given by

$$p=\rho A(\rho)v^2, \tag{17}$$

where $A(\rho)$ is a density-dependent function, and is defined as

$$A(\rho)=A_0+\delta A\left[1+\tanh\left(\frac{\rho-\rho_{cr}}{\delta\rho}\right)\right]. \tag{18}$$

Here A_0, δA and $\delta\rho$ are parameters.

In model (16), v_e is generalized equilibrium speed depending not only on the local state variables ρ and v but also on the variables ρ_a and v_a evaluated at the anticipated location x_a, where

$$\rho_a = \rho(x_a,t),\ \ v_a = v(x_a,t),\ \ x_a = x+\gamma(1/\rho_{\max}+Tv). \tag{19}$$

Here γ denotes an average anticipation factor and T is the safe time headway. The generalized equilibrium speed v_e can be defined by

$$v_e(\rho,v,\rho_a,v_a) = v_{\max}\left[1-\frac{A(\rho)}{A(\rho_{\max})}\left(\frac{\rho_a Tv}{1-\rho_a/\rho_{\max}}\right)^2 B(\delta_v)\right], \tag{20}$$

where $B(\delta_v)$ is a macroscopic interaction term

$$B(\delta_v) = 2\left[\delta_v\frac{e^{-\delta_v^2/2}}{\sqrt{2\pi}}+(1+\delta_v^2)\int_{-\infty}^{\delta_v}\frac{e^{-y^2/2}}{\sqrt{2\pi}}dy\right]. \tag{21}$$

Here $\delta_v = (v-v_a)/\sqrt{2A(\rho)v^2}$ is the dimensionless speed difference between the actual location x and the anticipated location x_a. The Jacobian matrix of the model (16) is given by

$$\mathbf{A(u)} = \begin{bmatrix} 0 & 1 \\ \rho v^2\dfrac{dA(\rho)}{d\rho}-A(\rho)v^2-v^2 & 2A(\rho)v+2v \end{bmatrix}. \tag{22}$$

The Jacobian matrix has the two real and distinct eigenvalues

$$\lambda_{1,2} = v\left(1+A(\rho)\pm\sqrt{A(\rho)^2+A(\rho)+\rho\,dA(\rho)/d\rho}\right). \tag{23}$$

An important characteristic of the GKT model is its non-local term, which is different from the above PW type and AR type macroscopic traffic flow models. The non-local term has smoothing properties like the viscosity term in some models. But the effect of the non-local term is forwardly directed, it is more realistic.

In GKT model, the steady-state speed-density relation $v_e(\rho)$ results from the implicit steady-state condition [17] and can be written as [56]

$$v_e(\rho) = \frac{\text{¶}^2}{2v_{\max}}\left(-1+\sqrt{1+\frac{4v_{\max}^2}{\text{¶}^2}}\right) \tag{24}$$

with

$$\text{¶} = \frac{1}{T}\left(\frac{1}{\rho}-\frac{1}{\rho_{\max}}\right)\sqrt{\frac{A(\rho_{\max})}{A(\rho)}}\,.$$

This also determines the equilibrium flow $q_e = \rho v_e(\rho)$. The equilibrium flow-density relation is shown in Fig. 3, in which the parameter values are as follows:

$A_0 = 0.008$, $\delta A = 0.02$, $\rho_{\max} = 0.16$ veh/m , $v_{\max} = 30.56$ m/s , $\delta\rho = 0.05\rho_{\max}$,

$\rho_{cr} = 0.27\rho_{\max}$, $T = 1.8$ s. (25)

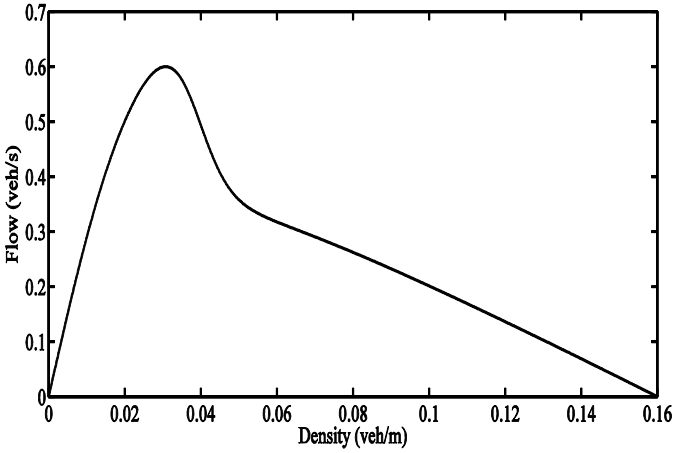

Fig. 3. Equilibrium flow-density relation of the GKT model.

Remark 1. Zhang [57] studied the link between driver memory in car-following and viscous effects in macroscopic traffic flow dynamics, and developed a second-order macroscopic model with viscosity, in which the momentum equation includes both the density gradient term and the speed gradient term. We do not study the numerical method for this model here.

3. Central-upwind approximation for traffic flow models

3.1. Semi-discrete central-upwind flux

For simplicity, let us consider a uniform grid: $x_\alpha = \alpha\Delta x$ and $t^n = n\Delta t$. The cell average of **u** in the spatial cell $I_j = [x_{j-\frac{1}{2}}, x_{j+\frac{1}{2}}]$ at time t^n is denoted by

$\bar{\mathbf{u}}_j^n = \frac{1}{\Delta x}\int_{I_j} \mathbf{u}(x,t^n)dx$. We assume that the cell-averages $\bar{\mathbf{u}}_j^n$ are available and use these cell-averages to reconstruct a piecewise polynomial interpolant:

$$\tilde{\mathbf{u}}(x) = \sum\nolimits_j \mathbf{h}_j(x)\chi_j(x), \tag{26}$$

where χ_j is the characteristic function of the interval I_j, and $\mathbf{h}_j(x)$ is a suitable degree polynomial in I_j which may be discontinuous at the cell interfaces $\{x_{j+\frac{1}{2}}\}$. The left- and right-sided local speeds of propagation of the discontinuities can be estimated by:

$$a^-_{j+1/2} = \min_{\omega\in C(\mathbf{u}^-_{j+1/2},\mathbf{u}^+_{j+1/2})}\left\{\lambda_1\left(\frac{\partial \mathbf{f}}{\partial \mathbf{u}}(\omega)\right),0\right\},\quad a^+_{j+1/2} = \max_{\omega\in C(\mathbf{u}^-_{j+1/2},\mathbf{u}^+_{j+1/2})}\left\{\lambda_N\left(\frac{\partial \mathbf{f}}{\partial \mathbf{u}}(\omega)\right),0\right\}, \tag{27}$$

where $\lambda_1 < \lambda_2 < \cdots < \lambda_N$ are the N eigenvalues of the Jacobian $\frac{\partial \mathbf{f}}{\partial \mathbf{u}}$, and $\mathbf{u}^-_{j+\frac{1}{2}}$ and $\mathbf{u}^+_{j+\frac{1}{2}}$ are the left and right point values of the reconstruction $\tilde{\mathbf{u}}(x)$, respectively:

$$\mathbf{u}^-_{j+\frac{1}{2}} = \mathbf{h}_j(x_{j+\frac{1}{2}}),\quad \mathbf{u}^+_{j+\frac{1}{2}} = \mathbf{h}_{j+1}(x_{j+\frac{1}{2}}). \tag{28}$$

In Eq. (27), $C(\mathbf{u}^-_{j+\frac{1}{2}},\mathbf{u}^+_{j+\frac{1}{2}})$ represents the curve that connects $\mathbf{u}^-_{j+\frac{1}{2}}$ with $\mathbf{u}^+_{j+\frac{1}{2}}$ in the phase space. In the genuinely nonlinear or linearly degenerate case, the local speeds can be computed by

$$a^-_{j+\frac{1}{2}} = \min\left\{\lambda_1\left(\frac{\partial \mathbf{f}}{\partial \mathbf{u}}(\mathbf{u}^-_{j+\frac{1}{2}})\right),\lambda_1\left(\frac{\partial \mathbf{f}}{\partial \mathbf{u}}(\mathbf{u}^+_{j+\frac{1}{2}})\right),0\right\},\quad a^+_{j+\frac{1}{2}} = \max\left\{\lambda_N\left(\frac{\partial \mathbf{f}}{\partial \mathbf{u}}(\mathbf{u}^-_{j+\frac{1}{2}})\right),\lambda_N\left(\frac{\partial \mathbf{f}}{\partial \mathbf{u}}(\mathbf{u}^+_{j+\frac{1}{2}})\right),0\right\}. \tag{29}$$

These local speeds of propagation are utilized to define the non-uniform space-time control volumes. Then, the solution is evolved to the next time level. The obtained solution is projected back onto the original grid, which leads to a fully discrete CU scheme. Further details can be found in [33]. A semi-discrete CU scheme can be obtained as $\Delta t \to 0$:

$$\frac{d}{dt}\bar{\mathbf{u}}_j(t) = -\frac{H_{j+\frac{1}{2}}(t) - H_{j-\frac{1}{2}}(t)}{\Delta x} + \bar{\mathbf{s}}_j(t), \tag{30}$$

where the numerical flux $H_{j+\frac{1}{2}}(t)$ has the form

$$H_{j+\frac{1}{2}}(t) = \frac{a^+_{j+\frac{1}{2}}\mathbf{f}(\mathbf{u}^-_{j+\frac{1}{2}}(t)) - a^-_{j+\frac{1}{2}}\mathbf{f}(\mathbf{u}^+_{j+\frac{1}{2}}(t))}{a^+_{j+\frac{1}{2}} - a^-_{j+\frac{1}{2}}} + \frac{a^+_{j+\frac{1}{2}}a^-_{j+\frac{1}{2}}}{a^+_{j+\frac{1}{2}} - a^-_{j+\frac{1}{2}}}\left(\mathbf{u}^+_{j+\frac{1}{2}}(t) - \mathbf{u}^-_{j+\frac{1}{2}}(t)\right), \tag{31}$$

and $\overline{\mathbf{s}}_j(t)$ is the discretization of the cell averages of the source term $\mathbf{s}$:

$$\overline{\mathbf{s}}_j(t) \approx \frac{1}{\Delta x}\int_{I_j} \mathbf{s}(\mathbf{u}(x,t))dx. \tag{32}$$

3.2. High-order reconstruction for spatial discretization

The choice of an appropriate reconstruction is a core step for spatial discretization, since the non-oscillatory behavior of the scheme depends on the reconstruction and the spatial order of the scheme also depends on the order of the reconstruction. In [33], the piecewise constant reconstruction and the piecewise linear reconstruction are applied and the first-order scheme and second-order scheme are developed. We here implement two high-order reconstructions for spatial discretization.

3.2.1. WENO reconstruction

We first apply an improved fifth-order WENO (WENOZ) reconstruction introduced by Borges et al. [58] to approximate the point values $\mathbf{u}^{\mp}_{j\pm\frac{1}{2}}$. The WENOZ method introduces new stiffness indicators to decrease the numerical dissipation and improve the resolution.

Considering a five-point stencil, i.e., $S=\left\{x_{j-2},x_{j-1},x_j,x_{j+1},x_{j+2}\right\}$, which is subdivided into three substencils:

$$S_k(j)=\left\{x_{j-k},x_{j-k+1},x_{j-k+2}\right\},\ k=0,1,2. \tag{33}$$

Then, the point value $\mathbf{u}^{-}_{j+\frac{1}{2}}$ is approximated by a convex combination of three interpolation polynomial defined in each substencil:

$$u^{-}_{j+\frac{1}{2}} = h_j(x_{j+\frac{1}{2}}) = \sum_{k=0}^{2}\omega_k^{-}h_{k,j}^{-}, \tag{34}$$

where

$$h_{0,j}^{-}=\frac{1}{3}\overline{u}_j+\frac{5}{6}\overline{u}_{j+1}-\frac{1}{6}\overline{u}_{j+2},\ h_{1,j}^{-}=-\frac{1}{6}\overline{u}_{j-1}+\frac{5}{6}\overline{u}_j+\frac{1}{3}\overline{u}_{j+1},\ h_{2,j}^{-}=\frac{1}{3}\overline{u}_{j-2}-\frac{7}{6}\overline{u}_{j-1}+\frac{11}{6}\overline{u}_j,$$

and $u^{-}_{j+\frac{1}{2}}$ and h_j are the i-th components of $\mathbf{u}^{-}_{j+\frac{1}{2}}$ and $\mathbf{h}_j$, respectively. In Eq. (34), the weights ω_k^{-} are defined by

$$\omega_k^{-}=\frac{\alpha_k^{-}}{\sum_{l=1}^{3}\alpha_l^{-}},\ \alpha_k^{-}=d_k\left[1+\left(\frac{\tau_5}{IS_k+\varepsilon}\right)\right],\ \tau_5=\left|IS_0-IS_2\right|,\ k=0,1,2, \tag{35}$$

where $d_0 = \frac{3}{10}$, $d_1 = \frac{3}{5}$, $d_2 = \frac{1}{10}$, and ε is a small number that is used to prevent the denominators becoming zero. In our simulations, ε is set to 10^{-40}. The smoothness indicators IS_k are given as follows:

$$
\begin{aligned}
IS_0 &= \frac{13}{12}(\bar{u}_j - 2\bar{u}_{j+1} + \bar{u}_{j+2})^2 + \frac{1}{4}(3\bar{u}_j - 4\bar{u}_{j+1} + \bar{u}_{j+2})^2, \\
IS_1 &= \frac{13}{12}(\bar{u}_{j-1} - 2\bar{u}_j + \bar{u}_{j+1})^2 + \frac{1}{4}(\bar{u}_{j-1} - \bar{u}_{j+1})^2, \\
IS_2 &= \frac{13}{12}(\bar{u}_{j\text{-}2} - 2\bar{u}_{j\text{-}1} + \bar{u}_j)^2 + \frac{1}{4}(3\bar{u}_{j\text{-}2} - 4\bar{u}_{j\text{-}1} + \bar{u}_j)^2.
\end{aligned} \tag{36}
$$

The reconstruction of $\mathbf{u}^+_{j-\frac{1}{2}}$ can be obtained by symmetry.

3.2.2. MP reconstruction

The second reconstruction we adopt is the fifth-order monotonicity preserving (MP5) reconstruction proposed by Suresh and Huynh [59]. The MP method applies the limiters to a high-order polynomial reconstruction in order to preserve monotonicity and accuracy. There are two major steps in the MP5 construction procedure.

In the first step, a fifth-order interpolation based on the same stencil as the WENOZ construction is constructed

$$
u^-_{j+\frac{1}{2}} = h_j(x_{j+\frac{1}{2}}) = \frac{1}{60}\left(2\bar{u}_{j-2} - 13\bar{u}_{j-1} + 47\bar{u}_j + 27\bar{u}_{j+1} - 3\bar{u}_{j+2}\right). \tag{37}
$$

This interface value is called the original value in [59]. We then compute the upper limit u^{UL} and the monotonicity-preserving value u^{MP}:

$$
u^{UL} = \bar{u}_j + \alpha(\bar{u}_j - \bar{u}_{j+1}), \tag{38}
$$

$$
u^{MP} = \bar{u}_j + \min\,\mathrm{mod}(\bar{u}_{j+1} - \bar{u}_j, \alpha(\bar{u}_j - \bar{u}_{j-1})), \tag{39}
$$

where $\alpha \geq 2$ is a constant and the minmod function is defined by

$$
\begin{aligned}
&\min\,\mathrm{mod}(z_1, \cdots, z_k) = s\min(|z_1|, \cdots, |z_k|), \\
&s = \frac{1}{2}(\mathrm{sgn}(z_1) + \mathrm{sgn}(z_2))\left|\frac{1}{2}(\mathrm{sgn}(z_1) + \mathrm{sgn}(z_3)) \cdots \frac{1}{2}(\mathrm{sgn}(z_1) + \mathrm{sgn}(z_k))\right|.
\end{aligned} \tag{40}
$$

Let $I(z_1, \cdots, z_k)$ denotes the interval $[\min(z_1, \cdots, z_k), \max(z_1, \cdots, z_k)]$. If the original

value lies in the monotonicity-preserving interval $I[\bar{u}_j, u^{MP}]$, which is the intersection of $I[\bar{u}_j, \bar{u}_{j+1}]$ and $I[\bar{u}_j, u^{UL}]$, such that

$$\left(u^{-}_{j+\frac{1}{2}} - \bar{u}_j\right)\left(u^{-}_{j+\frac{1}{2}} - u^{MP}\right) \le 0, \tag{41}$$

then the interface value is not changed.

In the second step, if the criterion (41) is not satisfied, it is necessary to apply the limiter to the original interface value given by Eq. (37). According to Suresh and Huynh [59], the intervals $I[\bar{u}_j, \bar{u}_{j+1}]$ and $I[\bar{u}_j, u^{MP}]$ are enlarged to $I[\bar{u}_j, \bar{u}_{j+1}, u^{MD}]$ and $I[\bar{u}_j, u^{MP}, u^{LC}]$, respectively, where

$$u^{MD} = \frac{1}{2}(\bar{u}_j + \bar{u}_{j+1}) - \frac{1}{2} D^{M4}_{j+\frac{1}{2}}, \tag{42}$$

$$u^{LC} = \bar{u}_j + \frac{1}{2}(\bar{u}_j - \bar{u}_{j-1}) + \frac{4}{3} D^{M4}_{j-\frac{1}{2}}. \tag{43}$$

Here $D^{M4}_{j+\frac{1}{2}} = \min\mathrm{mod}(4d_j - d_{j+1}, 4d_{j+1} - d_j, d_j, d_{j+1})$ and $d_j = \bar{u}_{j+1} - 2\bar{u}_j + \bar{u}_{j-1}$. The interval $I[u_{\min}, u_{\max}]$, which is the intersection of the two intervals $I[\bar{u}_j, \bar{u}_{j+1}, u^{MD}]$ and $I[\bar{u}_j, u^{MP}, u^{LC}]$, can be obtained, where

$$u_{\min} = \max(\min(\bar{u}_j, \bar{u}_{j+1}, u^{MD}), \min(\bar{u}_j, u^{UL}, u^{LC})), \tag{44}$$

$$u_{\max} = \min(\max(\bar{u}_j, \bar{u}_{j+1}, u^{MD}), \max(\bar{u}_j, u^{UL}, u^{LC})). \tag{45}$$

Then, the limiter is implemented and $u^{-}_{j+\frac{1}{2}}$ is replaced:

$$u^{-}_{j+\frac{1}{2}} \leftarrow u^{-}_{j+\frac{1}{2}} + \min\mathrm{mod}(u_{\min} - u^{-}_{j+\frac{1}{2}}, u_{\max} - u^{-}_{j+\frac{1}{2}}). \tag{46}$$

For more details about the derivation of the MP5 reconstruction, we refer to [59].

3.3. Time and source terms discretization

The time discretization of the semi-discrete scheme (30) requires a stable and an appropriate order. In our numerical simulations, we employ the third-order strong stability preserving (SSP) Runge-Kutta method [60]:

$$\mathbf{u}^{(1)} = \mathbf{u}^n + \Delta t L(\mathbf{u}^n),$$

$$\mathbf{u}^{(2)} = \frac{3}{4}\mathbf{u}^n + \frac{1}{4}\mathbf{u}^{(1)} + \frac{1}{4}\Delta t L(\mathbf{u}^{(1)}),$$

$$\mathbf{u}^{n+1} = \frac{1}{3}\mathbf{u}^n + \frac{2}{3}\mathbf{u}^{(2)} + \frac{2}{3}\Delta t L(\mathbf{u}^{(2)}). \tag{47}$$

The source terms $\overline{\mathbf{s}}_j(t)$ is approximated by the Simpson's quadrature rule, yielding

$$\overline{\mathbf{s}}_j(t) = \frac{1}{6}(\mathbf{s}(\mathbf{u}^+_{j-\frac{1}{2}}) + 4\,\mathbf{s}(\mathbf{u}_j) + \mathbf{s}(\mathbf{u}^-_{j+\frac{1}{2}})), \tag{48}$$

where $\mathbf{u}_j = \mathbf{h}_j(x_j)$. For the MP5 reconstruction, we use the following formula to compute the component of $\mathbf{u}_j$ [61]:

$$u_j = h_j(x_j) = \frac{3}{640}\overline{u}_{j-2} - \frac{29}{480}\overline{u}_{j-1} + \frac{1067}{960}\overline{u}_j - \frac{29}{480}\overline{u}_{j+1} + \frac{3}{640}\overline{u}_{j+2}, \tag{49}$$

which is a fifth-order reconstruction to u_j. For the WENOZ reconstruction, we adopt the same method used for the WENO reconstruction [61] to compute u_j.

The choice of Δt is determined by the CFL condition

$$CFL = \frac{\Delta t}{\Delta x} a \le \frac{1}{2}, \quad a = \max_j \left\{ \max\left(-a^-_{j+\frac{1}{2}}, a^+_{j+\frac{1}{2}} \right) \right\}. \tag{50}$$

4. Numerical simulations

For simplicity, the CU schemes based on the WENOZ reconstruction and the MP5 reconstruction are abbreviated to the CU-WENOZ scheme and the CU-MP5 scheme, respectively. We compare the performance of the proposed CU-WENOZ and CU-MP5 schemes with the first-order scheme (CU1) and second-order scheme (CU2) which are obtained by using the piecewise constant interpolant and the piecewise linear reconstruction with the minmod limiter at the reconstruction step [33], respectively. In CU2 scheme, the parameter in the minmod limiter is taken to be 1.3. The parameter α in Eq. (39) is taken as 4.0 and the CFL number is set to 0.475, unless otherwise stated.

4.1. Numerical Examples for the PW model

We consider Riemann problems for the PW model and present several numerical examples. According to [4,22,48,49], there exist eight kinds of wave solutions of Riemann problems for the PW model without the relaxation term, which are 1-shock wave (S_1), 2-

shock wave (S_2), 1-rarefaction wave (R_1), 2-rarefaction wave (R_2), $S_1 - S_2$ (1-shock+2-shock) wave, $S_1 - R_2$ (1-shock+2-rarefaction) wave, $R_1 - S_2$ (1-rarefaction+2-shock) wave, and $R_1 - R_2$ (1-rarefaction+2-rarefaction) wave. The parameter values are given as follows:

$$\tilde{l} = 10\,\text{m},\ \tilde{\tau} = 10\,\text{s},\ L = 800\tilde{l},\ \rho_{\max} = 0.18\ \text{veh/m},\ c_0 = 2.48445\tilde{l}/\tilde{\tau}, \tag{51}$$

where L is the length of the road. The simulations are performed on a uniform grid with 400 grid points.

For the first case, the relaxation time in Eq. (3) is taken to be $1000\tilde{\tau}$, which is long enough such that 2-waves don't relax to 1-waves and we can observe the last four types of waves at final time. We use four Riemann initial conditions from Jin [22] and present the computed solutions at time $t = 500\,\text{s}$.

The first initial condition is given by

$$(\rho(x,0), v(x,0)) = \begin{cases} (\rho_l, v_l) = (0.16,\ v_e(0.16)), & x \le 4000, \\ (\rho_r, v_r) = (0.16 - 0.02,\ v_e(0.16)), & x > 4000. \end{cases} \tag{52}$$

For this case, the solutions are of $R_1 - S_2$ type. Figure 4 shows the density profile computed by the different schemes. The numerical results are plotted together with the reference solution, which is a converged solution calculated by the CU2 scheme with 6400 grid points. From Fig. 4, we can see that higher-order schemes yield more accurate solutions with high resolution, while the CU1 scheme generates excessive numerical dissipation. In comparison with the CU2 scheme, the CU-WENOZ scheme and the CU-MP5 scheme produce a better resolution, and the shock and rarefaction waves are well resolved by both schemes.

The second initial condition is

$$(\rho(x,0), v(x,0)) = \begin{cases} (\rho_l, v_l) = (0.16,\ v_e(0.16)), & x \le 4000, \\ (\rho_r, v_r) = (0.16,\ v_e(0.16) + 0.2), & x > 4000. \end{cases} \tag{53}$$

The solutions for this case are of $R_1 - R_2$ type. The numerical results are shown in Fig. 5, and it clearly illustrates the advantage of high-resolution schemes. In contrast, the CU-MP5

scheme provides slightly better result than the CU-WENOZ scheme, and both schemes offer better results than the CU2 scheme.

The third initial condition is

$$(\rho(x,0),v(x,0))=\begin{cases}(\rho_l,v_l)=(0.16,\, v_e(0.16)), & x\le 4000,\\ (\rho_r,v_r)=(0.16,\, v_e(0.16)-0.2), & x>4000.\end{cases} \tag{54}$$

For this case, the solutions are of S_1-S_2 type. The numerical results for the density profile are displayed in Fig. 6. From Fig. 6, we can see that the resolution of the CU2 scheme is better than that of the CU1 scheme but worse than that of the CU-WENOZ scheme and the CU-MP5 scheme. In contrast, the CU-WENOZ scheme generates the slight oscillation, while the CU-MP5 scheme performs well.

The fourth initial condition is

$$(\rho(x,0),v(x,0))=\begin{cases}(\rho_l,v_l)=(0.16,\, v_e(0.16)), & x\le 4000,\\ (\rho_r,v_r)=(0.16+0.02,\, v_e(0.16)), & x>4000.\end{cases} \tag{55}$$

The solutions for this case are of S_1-R_2 type. We show the numerical results of the density profile in Fig. 7. As it can be seen, the resolution achieved by high-order scheme is better. The CU-MP5 scheme gives a slightly better result, compared with the CU-WENOZ scheme.

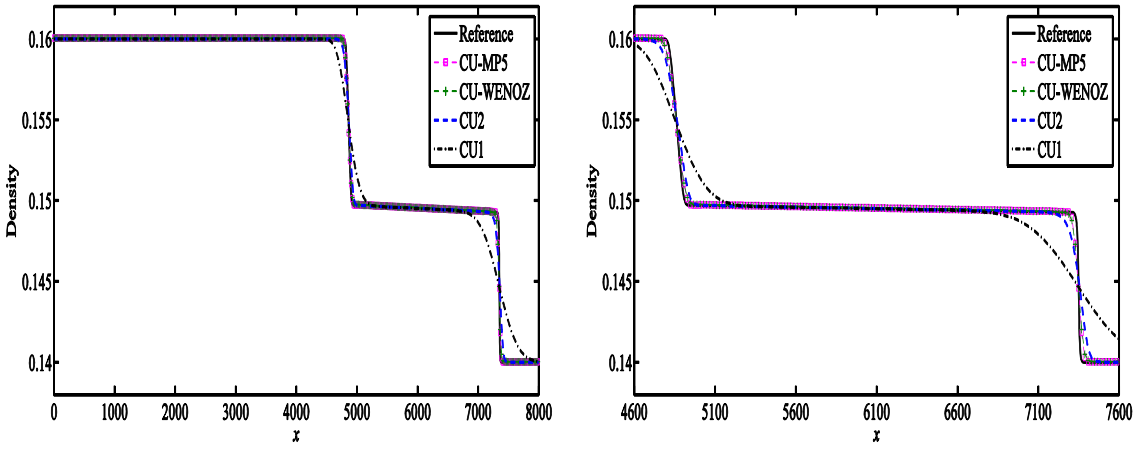

(a) (b)

Fig. 4. Results for the PW model with the initial data (52). (a) Density; (b) Zoomed region of (a).

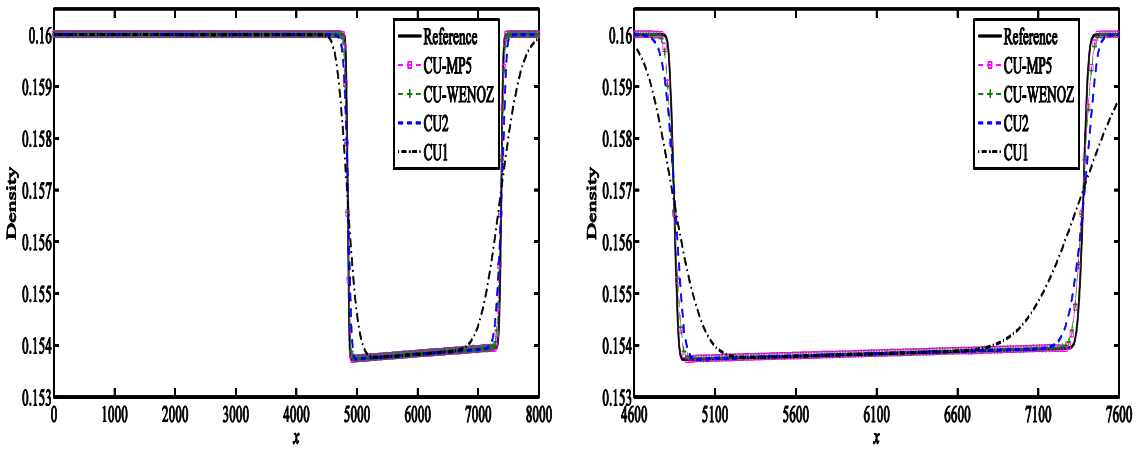

Fig. 5. Results for the PW model with the initial data (53). (a) Density; (b) zoomed region of (a).

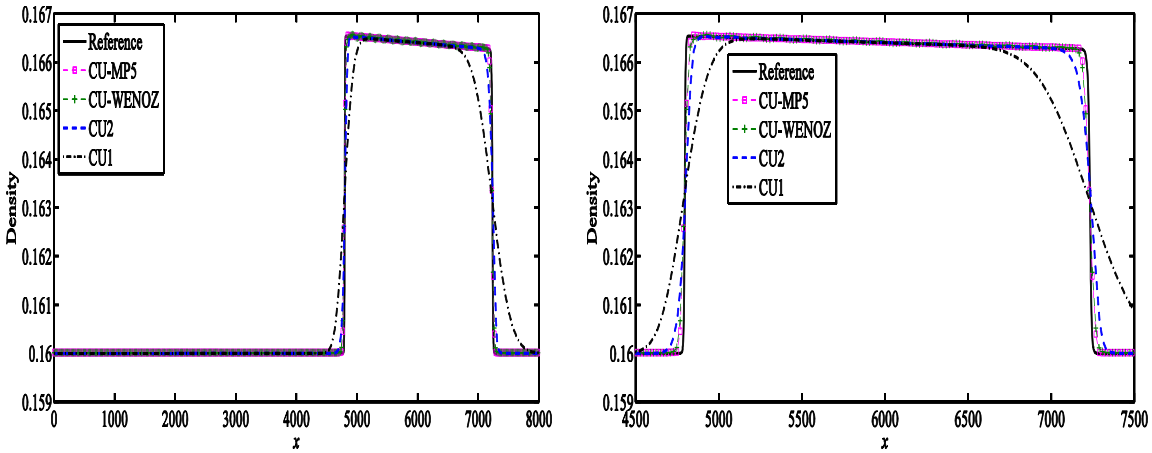

Fig. 6. Results for the PW model with the initial data (54). (a) Density; (b) zoomed region of (a).

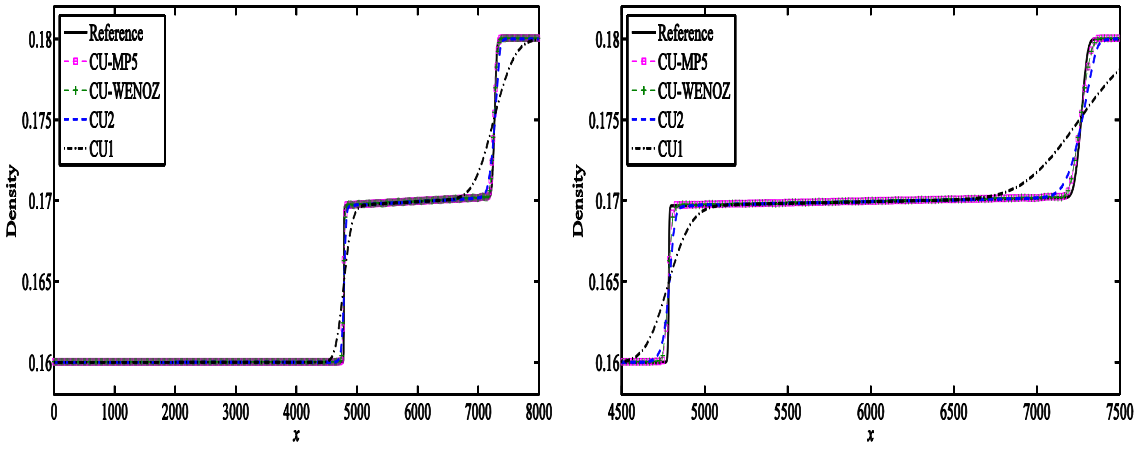

Fig. 7. Results for the PW model with the initial data (55). (a) Density; (b) zoomed region of (a).

In the second case, we use the same initial conditions as the first case, but change the relaxation time in Eq. (3) to $2\tilde{\tau}$, which is much shorter such that 2-waves relax to 1-waves

due to the effect of the source term. Other parameter values are the same as those used in the first case.

For the initial condition (52), the results computed by three schemes are presented in Figs. 8-10. In this situation, a new R_1 wave forms when the S_2 wave disappears. The traffic flow will become uniform as these two rarefaction waves propagate. This transition and the propagation of the two rarefaction waves are well resolved by the CU-WENOZ scheme and the CU-MP5 scheme. Both schemes accurately capture fine details of the flow, and they are superior to the CU1 scheme.

For the initial condition (53), the numerical results are shown in Figs. 11-13. In this situation, a downstream shock S_1 forms as the traffic flow relaxes to the equilibrium state at around $t = 2\tilde{\tau}$, and then a free region with higher travel speed and lower density is formed. This free region gradually disappears as the waves propagate, and the traffic will become uniform. The results shown in Figs. 11-13 illustrate that the CU-WENOZ scheme and the CU-MP5 scheme achieve a high resolution, while the CU1 scheme cannot provide fine details of the flow. The CU-MP5 scheme gives a slightly sharper resolution, compared with the CU-WENOZ scheme.

For the initial condition (54), the numerical results are displayed in Figs. 14-16. In this situation, the S_2 wave disappears and a R_1 wave forms at around $t = 2\tilde{\tau}$, and then a cluster with lower travel speed and higher density is formed. The traffic flow will eventually become uniform as the waves propagate. The formation and propagation of the cluster are well resolved by both high-order schemes and the CU-MP5 scheme produces a slightly sharper resolution. Again, the CU1 scheme fails to capture fine details of the flow with the same grid.

For the initial condition (55), the numerical results are illustrated in Figs. 17-19. In this situation, a new S_1 wave forms when the R_2 wave disappears. The formation and propagation of the waves are well predicted by both high-order schemes and produce a sharp resolution.

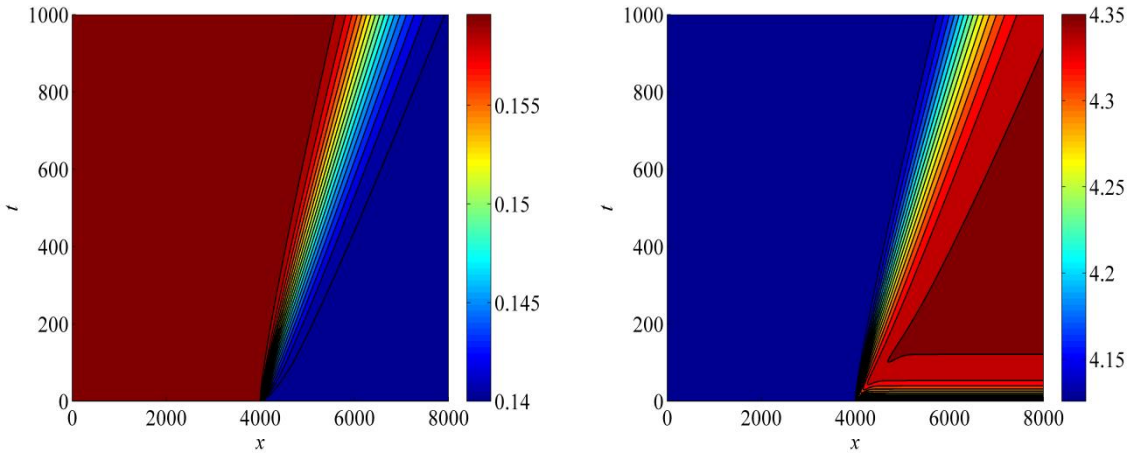

(a) (b)

Fig. 8. Evolution of density and velocity for the PW model with the initial data (52) computed by the CU1 scheme. (a) Density; (b) Velocity.

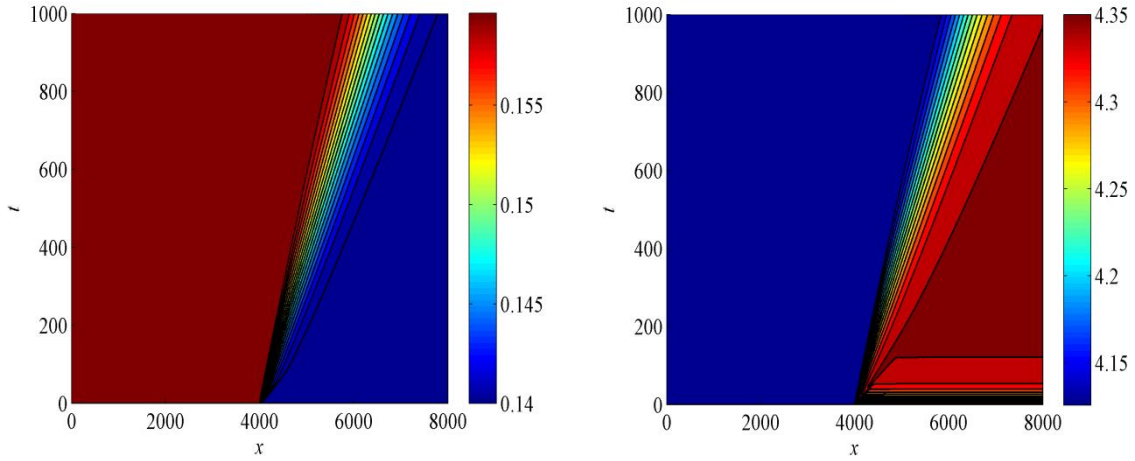

(a) (b)

Fig. 9. Evolution of density and velocity for the PW model with the initial data (52) computed by the CU-MP5 scheme. (a) Density; (b) Velocity.

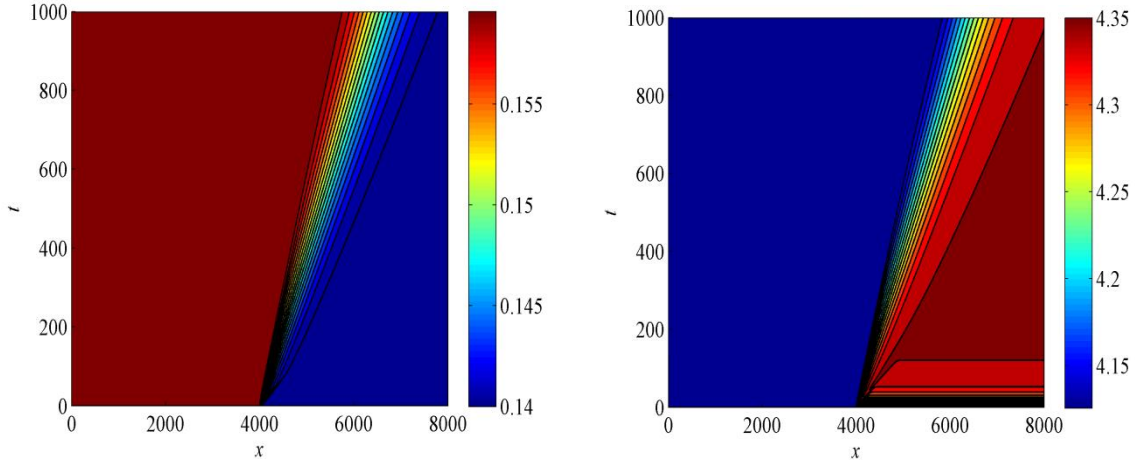

(a) (b)

Fig. 10. Evolution of density and velocity for the PW model with the initial data (52) computed by the CU-WENOZ scheme. (a) Density; (b) Velocity.

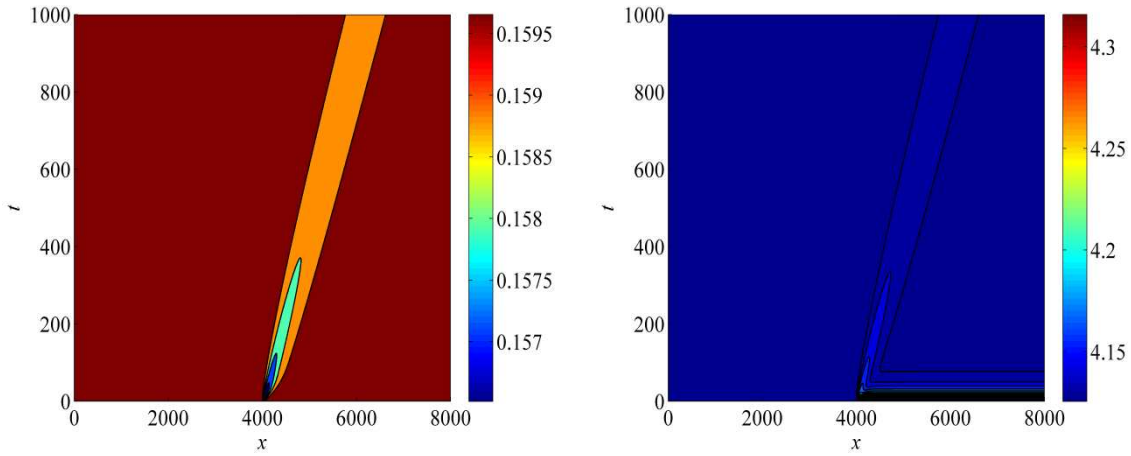

(a) (b)

Fig. 11. Evolution of density and velocity for the PW model with the initial data (53) computed by the CU1 scheme. (a) Density; (b) Velocity.

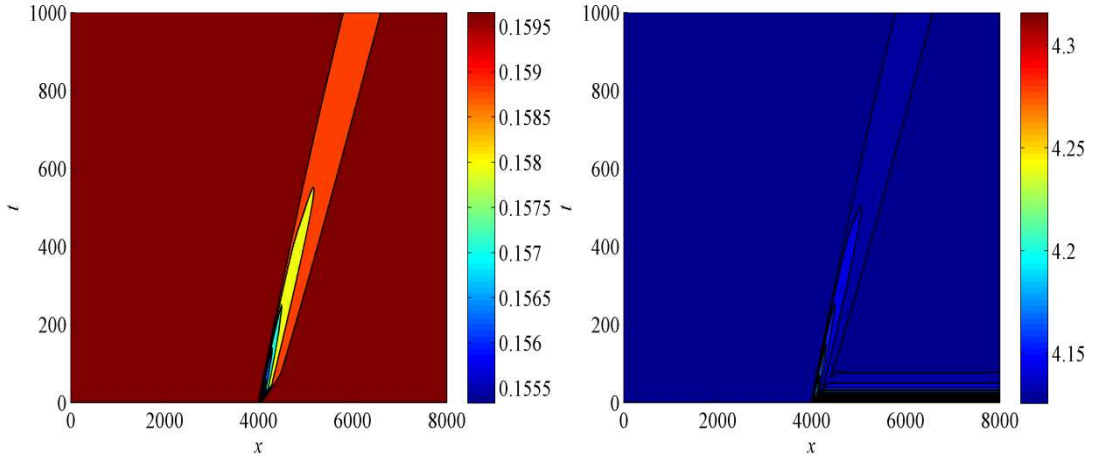

(a) (b)

Fig. 12. Evolution of density and velocity for the PW model with the initial data (53) computed by the CU-MP5 scheme. (a) Density; (b) Velocity.

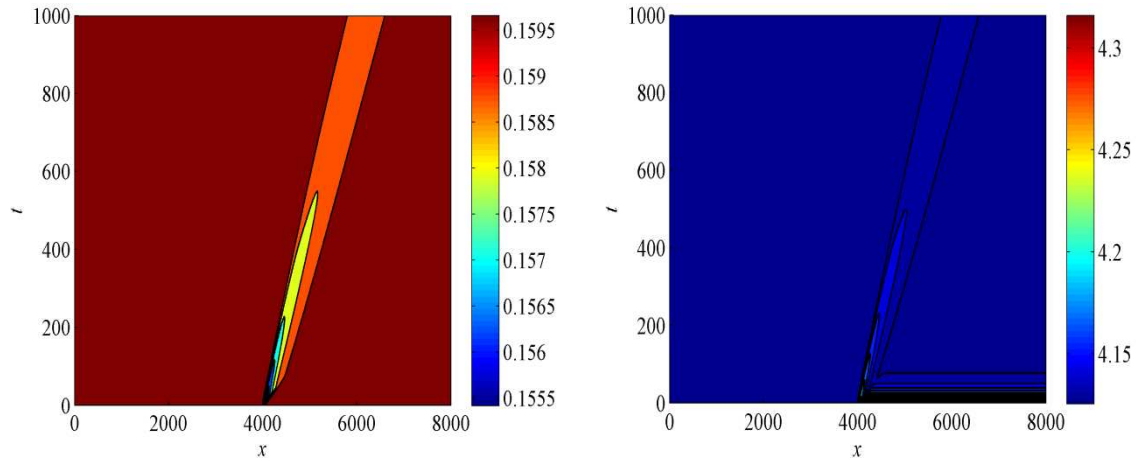

(a) (b)

Fig. 13. Evolution of density and velocity for the PW model with the initial data (53) computed by the CU-WENOZ scheme. (a) Density; (b) Velocity.

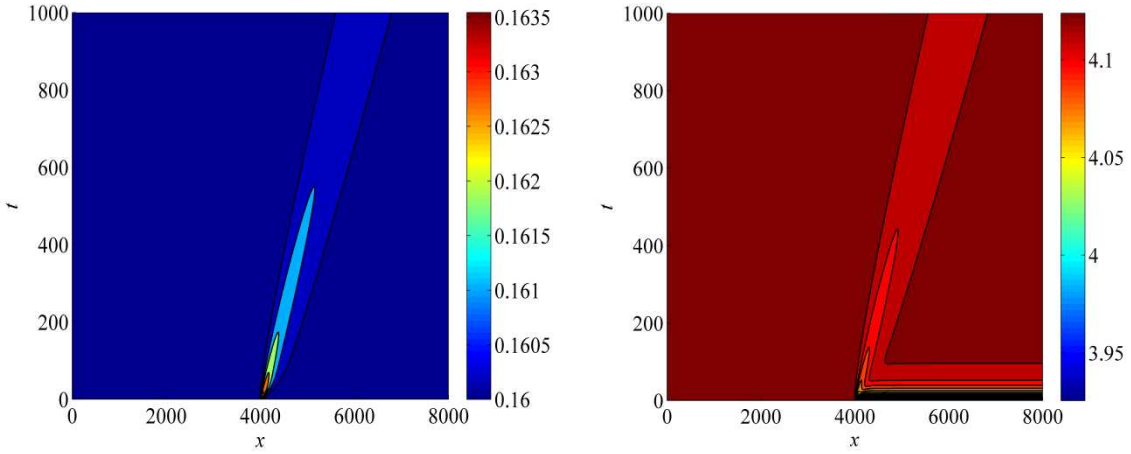

(a) (b)

Fig. 14. Evolution of density and velocity for the PW model with the initial data (54) computed by the CU1 scheme. (a) Density; (b) Velocity.

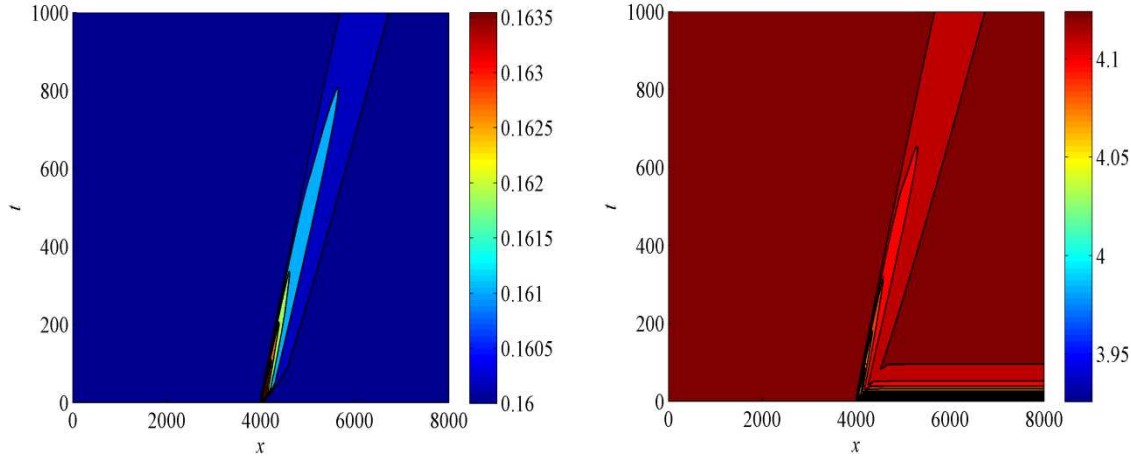

(a) (b)

Fig. 15. Evolution of density and velocity for the PW model with the initial data (54) computed by the CU-MP5 scheme. (a) Density; (b) Velocity.

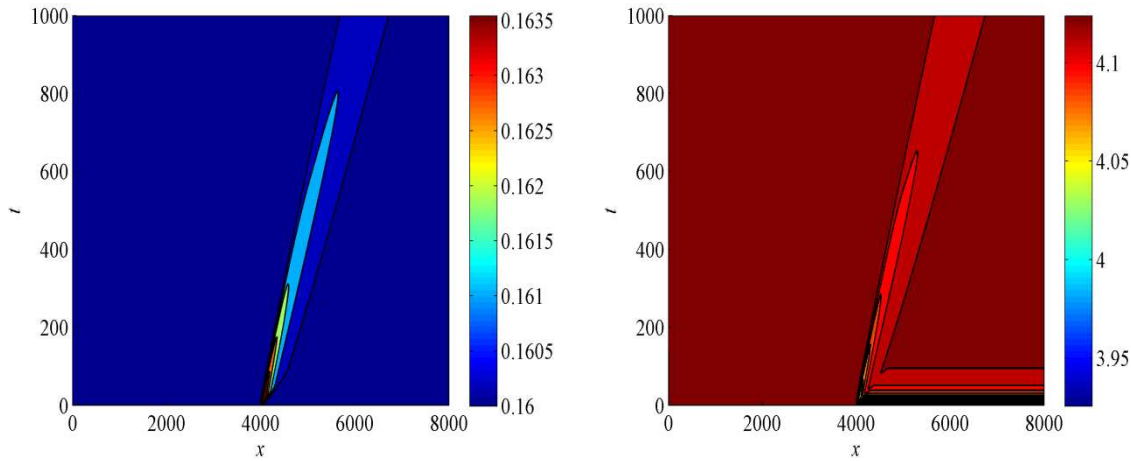

(a) (b)

Fig. 16. Evolution of density and velocity for the PW model with the initial data (54) computed by the CU-WENOZ scheme. (a) Density; (b) Velocity.

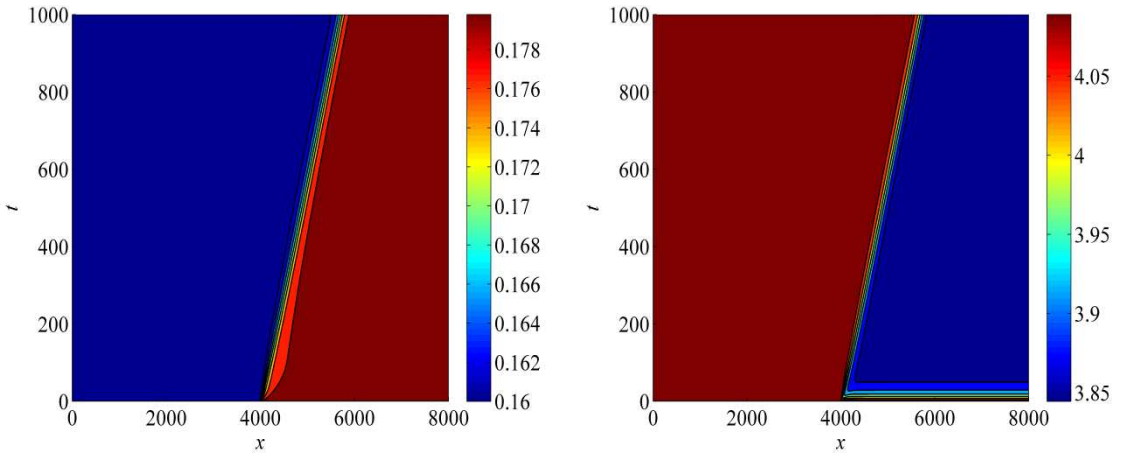

(a) (b)

Fig. 17. Evolution of density and velocity for the PW model with the initial data (55) computed by the CU1 scheme. (a) Density; (b) Velocity.

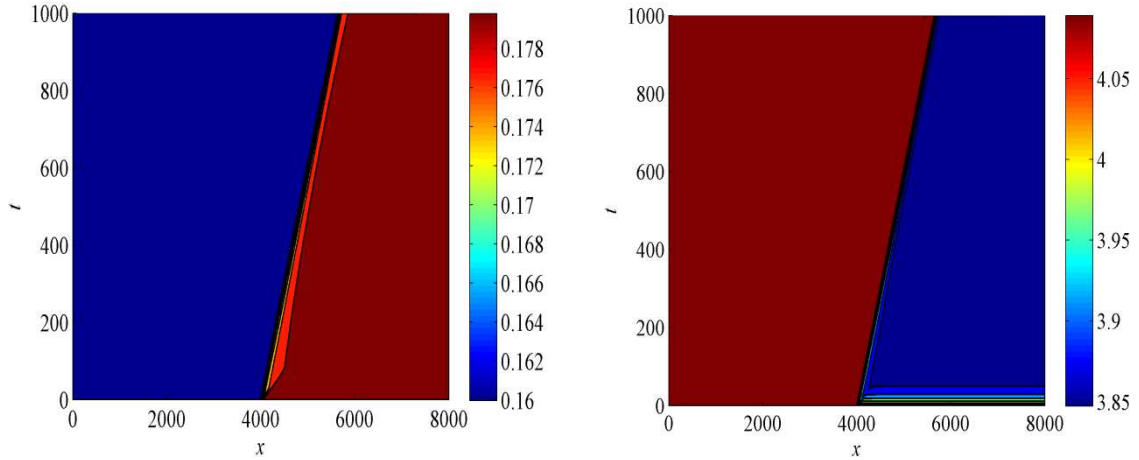

(a) (b)

Fig. 18. Evolution of density and velocity for the PW model with the initial data (55) computed by the CU-MP5 scheme. (a) Density; (b) Velocity.

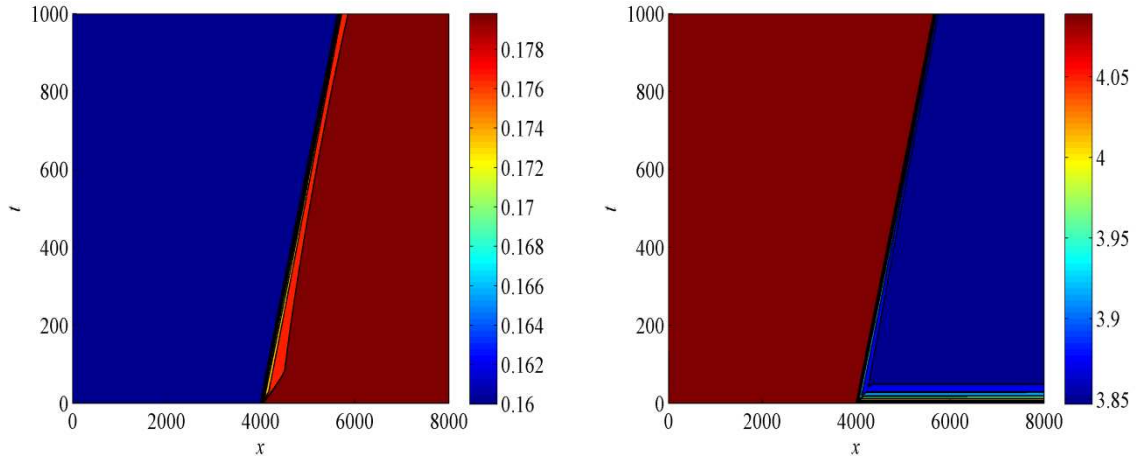

(a) (b)

Fig. 19. Evolution of density and velocity for the PW model with the initial data (55) computed by the CU-WENOZ scheme. (a) Density; (b) Velocity.

4.2. Numerical Examples for the AR model

In this subsection, we present the numerical results for the AR model. The computational domain is taken to be $[0,1]$ and we set $v_{\max}=1$ and $\rho_{\max}=1$.

For a convergence test of the proposed schemes, we first use the following initial data:

$$\rho(x,0)=0.05+0.01\sin^4(2\pi x),\quad v(x,0)=0.9,$$

and set periodic boundary conditions. We choose the time step $\Delta t=4\Delta x^{5/3}$. Table 1 shows the L_1 errors and convergence rates at output time $t=0.2$. The errors in the L_1 norm are obtained by comparing the numerical solution with the reference solution which is computed by the same method with 1280 grid points. We can observe that the CU-MP5 scheme achieves close fifth-order convergence. The CU-MP5 scheme gives more accurate numerical solutions than the CU-WENOZ scheme for this problem.

The second initial condition we use is

$$(\rho(x,0),v(x,0))=\begin{cases}(\rho_l,v_l)=(0.5,0.6), & x\le 0.5,\\ (\rho_r,v_r)=(0.7,0.2), & x>0.5.\end{cases} \tag{56}$$

According to [8], the corresponding solution consists of a left-going shock wave followed by a contact discontinuity. The parameter α in Eq. (39) is set to 2.0. Figure 20 illustrates the spatiotemporal evolution of the density and velocity in a period of 0.4 computed by the CU-MP5 scheme with 400 grid points. Figure 21 gives a comparison of different schemes with the exact solution at $t=0.4$. We can see that the CU1 scheme produces excessive numerical dissipation, and the CU-WENOZ and the CU-MP5 schemes produce slightly better resolution than the CU2 scheme. In contrast, the CU-WENOZ scheme yields the slight oscillation while the CU-MP5 scheme performs well.

The third initial condition we consider is

$$(\rho(x,0),v(x,0))=\begin{cases}(\rho_l,v_l)=(0.7,0.3), & x\le 0.5,\\ (\rho_r,v_r)=(0.5,0.5), & x>0.5.\end{cases} \tag{57}$$

The solution of this case is given by a rarefaction wave followed by a contact discontinuity [8]. The parameter α in Eq. (39) is taken as 2.0. The spatiotemporal evolution of the numerical results obtained by the CU-MP5 scheme with 400 grid points is presented in Fig.

22. Figure 23 compares the numerical results with the exact solution at $t=0.4$. High-order schemes again achieve a better resolution. The CU-MP5 scheme provides a slightly better result, compared with the CU-WENOZ scheme.

The fourth initial condition is

$$(\rho(x,0),v(x,0))=\begin{cases}(\rho_l,v_l)=(0.2,0.2), & x\le 0.5,\\ (\rho_r,v_r)=(0.2,0.8), & x>0.5.\end{cases} \tag{58}$$

In this case, the solution consists of a rarefaction wave, followed by a fake vacuum wave and then by a contact discontinuity [1,8]. The appearance of the vacuum is a challenge test for any numerical method to resolve the transition to free flow regions. In Fig. 24, we give the numerical results of different schemes at $t=0.4$, which are compared with the exact solution. For this case, we use 800 grid points and the CFL number is set to 0.1. From Fig. 24, it can be seen that the appearance of the vacuum and the transition are better predicted by the CU-MP5 scheme and the CU-WENOZ scheme.

Table 1. Errors and orders of convergence for the CU-MP5 and CU-WENOZ schemes.

N	CU-MP5 scheme		CU-WENOZ scheme	
	L_1 error	L_1 order	L_1 error	L_1 order
20	1.4397E-04	–	1.5921E-04	–
40	6.2843E-06	4.52	8.3115E-06	4.26
80	2.1550E-07	4.87	5.6737E-07	3.87
160	7.8424E-09	4.78	2.8040E-08	4.34

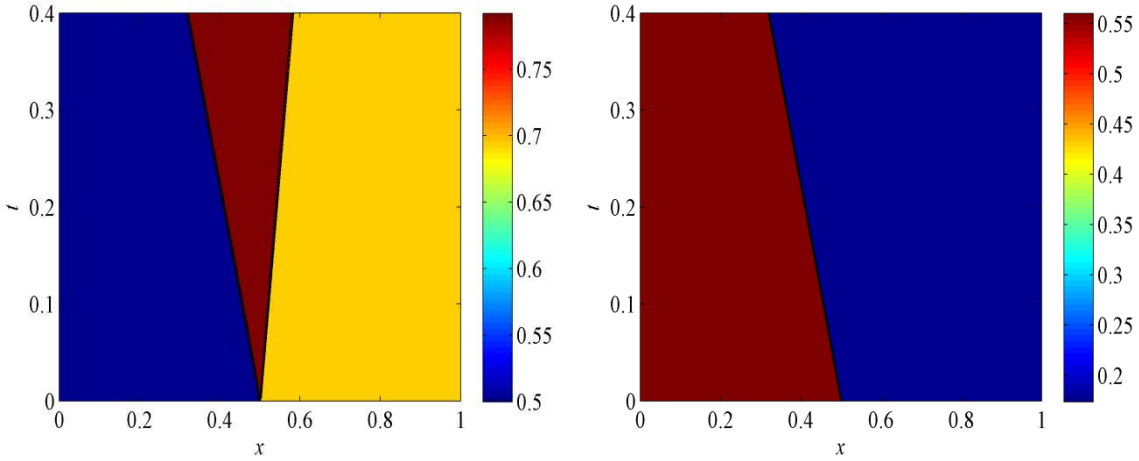

(a) (b)

Fig. 20. Evolution of density and velocity for AR model with the initial data (56) computed by the CU-MP5 scheme. (a) Density; (b) Velocity

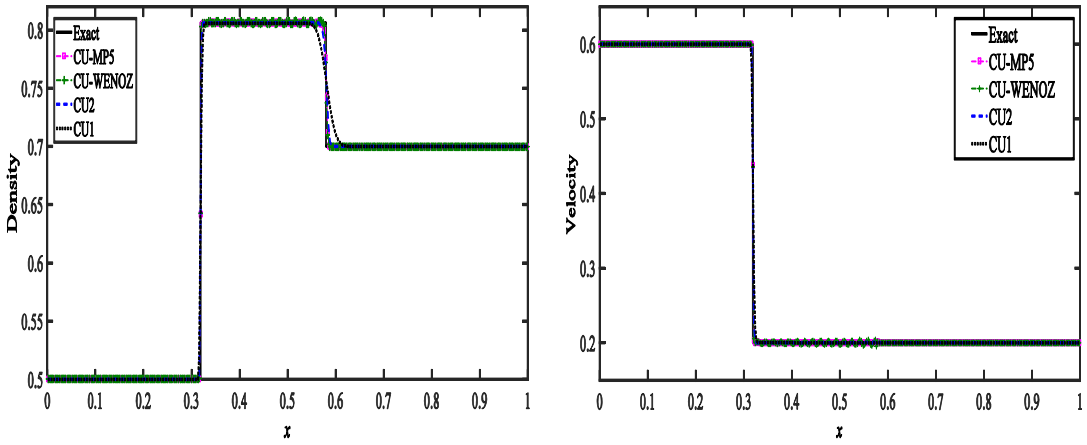

(a) (b)

Fig. 21. Results for the AR model with the initial data (56). (a) Density; (b) Velocity.

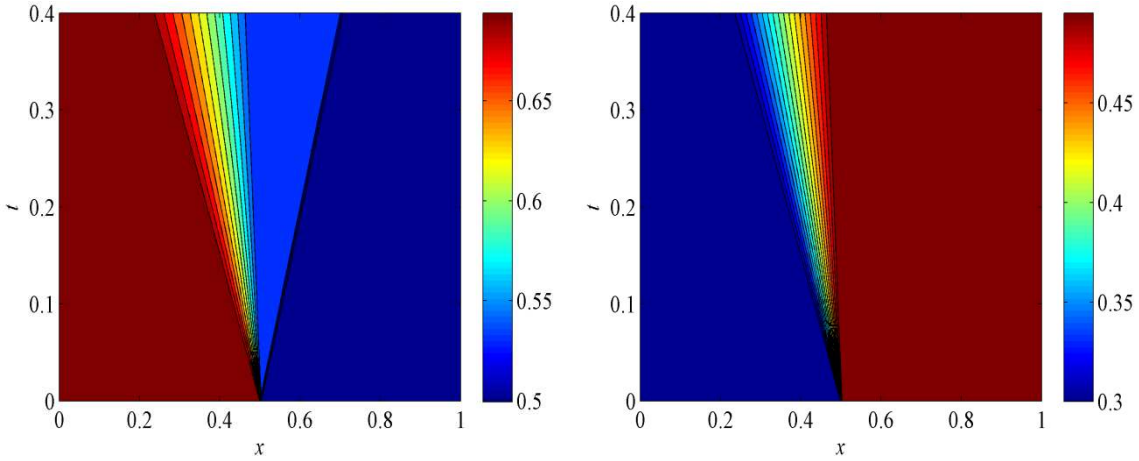

(a) (b)

Fig. 22. Evolution of density and velocity for AR model with the initial data (57) computed by the CU-MP5 scheme. (a) Density; (b) Velocity.

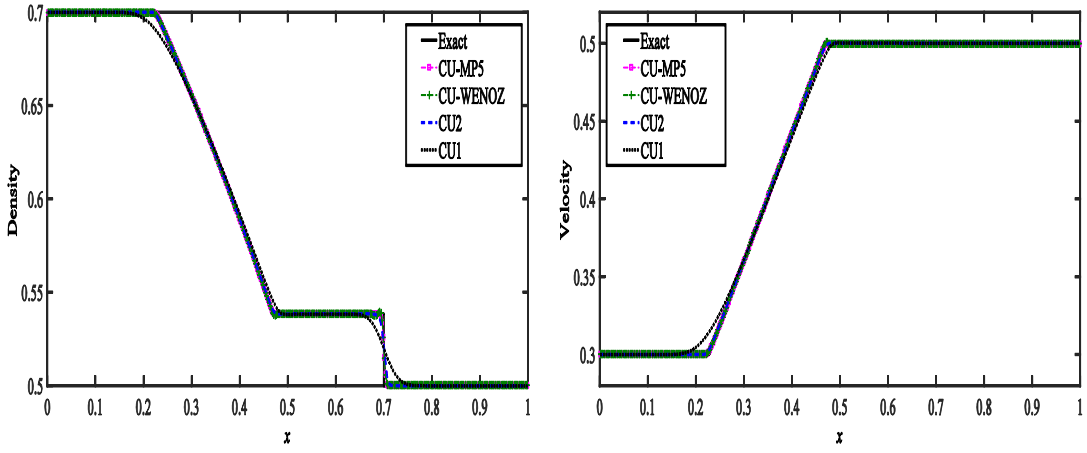

(a) (b)

Fig. 23. Results for the AR model with the initial data (57). (a) Density; (b) Velocity.

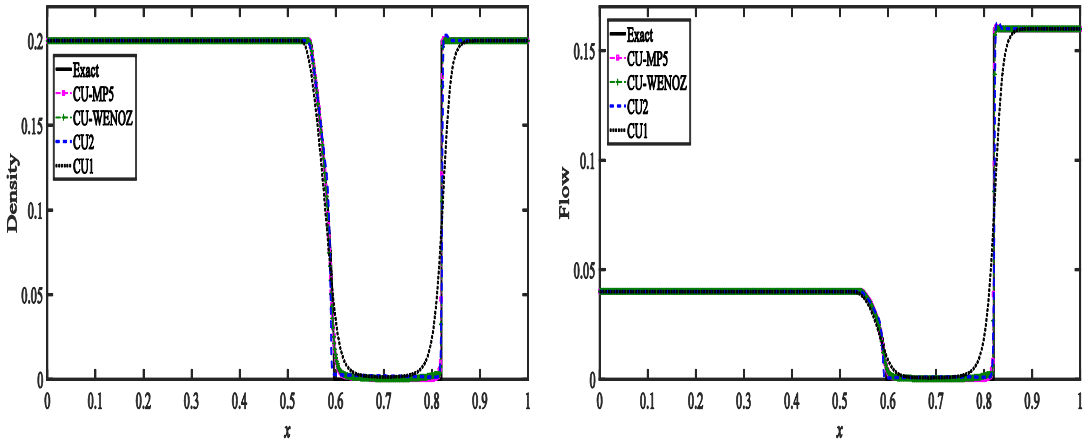

(a) (b)

Fig. 24. Results for the AR model with the initial data (58). (a) Density; (b) Velocity.

4.3. Numerical Examples for the Zhang model

In this subsection we present the numerical test for the Zhang model. The length of the road L is $8000\,\mathrm{m}$, and other parameter values used are given in (15).

The first case we consider has the following initial condition:

$$(\rho(x,0),v(x,0))=\begin{cases}(\rho_l,v_l)=(0.02,25.0), & x\le 4000,\\ (\rho_r,v_r)=(0.05,15.0), & x>4000.\end{cases} \tag{59}$$

This initial data satisfies the conditions $0\le v_r-v_l+v_e(\rho_l)\le v_{\max}$ and $v_r\le v_l$. According to Mammer et al. [55], the solution for this case contains a shock-wave followed by a contact discontinuity. In Fig. 25, the numerical results computed by all schemes at $t=200\mathrm{s}$ with 400 grid points are compared with the exact solution. One can observe that all schemes capture the correct solution. A good agreement with the exact solution is observed for high-order schemes. The CU-WENOZ and the CU-MP5 schemes produce better resolution than the CU1 scheme and the CU2 scheme.

The second initial condition we use is

$$(\rho(x,0),v(x,0))=\begin{cases}(\rho_l,v_l)=(0.1,5.0), & x\le 4000,\\ (\rho_r,v_r)=(0.08,10.0), & x>4000.\end{cases} \tag{60}$$

In this case, the initial data satisfies the conditions $0\le v_r-v_l+v_e(\rho_l)\le v_{\max}$ and $v_r>v_l$. According to Mammer et al. [55], the solution consists of a rarefaction wave followed by a contact discontinuity. The results are shown in Fig. 26. The solution is computed up to

$t = 300\text{s}$ with 400 grid points. As can be seen from Fig. 26, the numerical results are in good agreement with the exact solution for high-order schemes. Similar to the first case, the CU-WENOZ scheme and the CU-MP5 scheme provide better results.

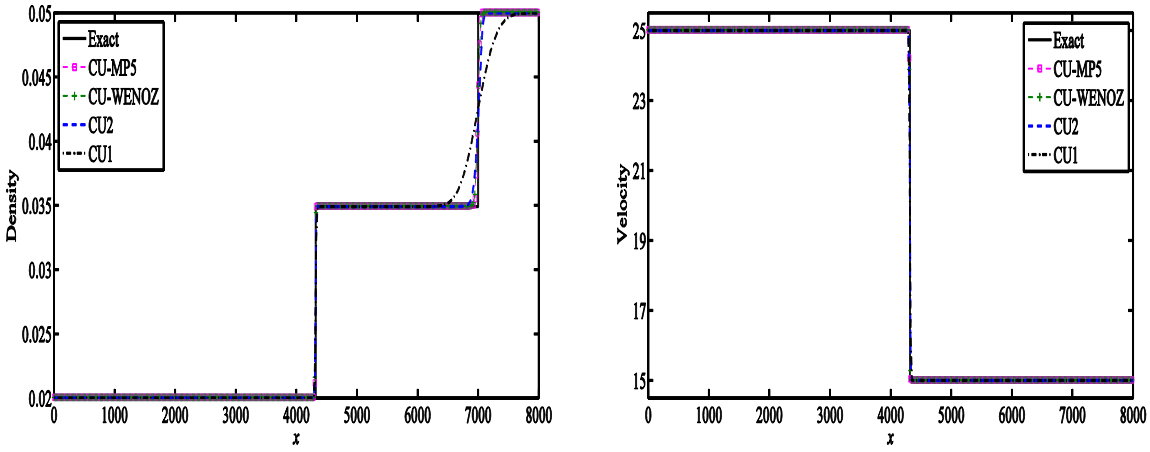

(a) (b)

Fig. 25. Results for the ARZ model with the initial data (59). (a) Density; (b) Velocity.

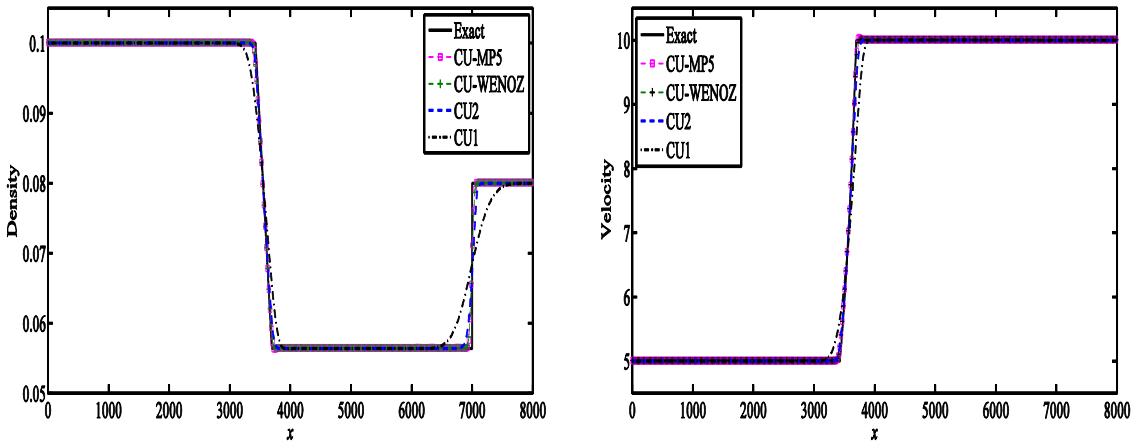

(a) (b)

Fig. 26. Results for the ARZ model with the initial data (60). (a) Density; (b) Velocity.

4.4. Numerical Example for the GKT model

In this subsection, we use a representative test to investigate the performance of the present scheme for the GKT model.

Following [16,56,62], we adopt the following dipole-like initial variation of the average density $\bar{\rho}$:

$$\rho(x,0) = \bar{\rho} + \Delta\rho\left\{\cosh^{-2}\left(\frac{x-x_0}{w^+}\right) - \frac{w^+}{w^-}\cosh^{-2}\left(\frac{x-x_0-\Delta x_0}{w^-}\right)\right\}, \tag{61}$$

where x_0 and $x_0 + \Delta x_0$ are, respectively, the positions of the positive and negative peaks, $w^+ = 201.25$ m, $w^- = 805$ m, $\Delta x_0 = w^+ + w^-$ and $\Delta\rho$ represents the amplitude of the perturbation. The initial flow is assumed to be in local equilibrium, i.e.,

$$q(x,0) = q_e(\rho(x,0)) = \rho v_e(\rho). \tag{62}$$

The periodic boundary condition is specified for this test. The length of the road L is 10000 m. The parameter values used are as follows:

$$\tau = 32 \text{ s}, \quad \gamma = 1.2. \tag{63}$$

Other parameter values used are given in (25). The amplitude of the perturbation $\Delta\rho$ is set to 0.006 veh/m and the average density $\bar{\rho}$ is varied in simulations.

Figure 27 illustrates the spatiotemporal evolution of the density for $\bar{\rho} = 0.015$ veh/m and $\bar{\rho} = 0.025$ veh/m using 400 grid points. The results are computed by the CU-MP5 scheme. When the traffic density is very low, the perturbation dissipates without amplification (see Fig. 27(a)). This means that the homogeneous traffic with a localized perturbation is stable at sufficiently low densities. As the density $\bar{\rho}$ increases to 0.025 veh/m, small perturbations are amplified and lead to traffic instability. In Fig. 27(b), we can see that a single density cluster forms.

When the initial density $\bar{\rho}$ continues to increase to 0.036 veh/m, a cascade of traffic jams appear, which corresponds to the stop-and-go traffic phenomenon. Figs. 28(a) and 28(b) show the results obtained by the CU-MP5 scheme using 400 and 800 grid points, respectively. Figs. 28(c) and 28(d) show the results of the CU1 scheme. We observe from Fig. 28(c) that the CU1 scheme fails to capture all the stop-and-go waves when 400 grid points are used. When we increase the grid points to 1600, the CU1 scheme can capture the structure of all waves (see Fig. 28(d)). This illustrates that high-order and high-resolution methods need fewer grid points to resolve the solution accurately.

Figure 29(a) shows that as the density is increased to 0.45, we can observe that a complex structure consisting of more clusters appears, but the amplitude of the clusters decreases comparing with Fig. 28(a). When the density increases even further, a stable congested traffic is reached (see Fig. 29(b)). The results in Fig. 29 are obtained using the CU-MP5 scheme with 400 grid points.

These results are similar to those reported and discussed in [16,29,32, 62].

We next study how sensitive are the numerical solutions to the GKT parameters. In (25) and (63), only one parameter is varied while keeping others unchanged. The results obtained using the CU-MP5 scheme with 400 grid points are shown in Fig. 30, where the numerical solution is computed up to $t = 1200\text{s}$. Fig. 30(a) illustrates the effect of the relaxation time. When $\tau = 19\text{s}$, the initial perturbation travels downstream and a stable flow is obtained. As τ is increased to 32s, a single cluster is formed. Increasing τ even further to 45s, the stop-and-go traffic appears. This indicates that the stability of traffic flow decreases with the increase of τ. The effect of the safe time headway T is shown in Fig. 30(b). When $T = 1.5$ and $T = 2.0$, a single local cluster forms for both cases, but the amplitude of the cluster for the case of $T = 2.0$ is smaller than that for the case of $T = 1.5$. As T is decreased to 1.0, stop-and-go traffic emerges. This means that the stability of traffic flow is improved by increasing the safe time headway. By the similar discussion, we can find that the stability of traffic flow increases with the increase of the anticipation factor γ or the desired velocity $v_{\max}$ (see Fig. 30(c) and Fig. 30(d)). These results are consistent with the theory results presented in [17]. Fig. 30(e) shows that the decrease of δA can increase the stability of traffic flow.

Remark 2. For the GKT model, we need to calculate the anticipated variables ρ_a and v_a in (19) at the anticipated position x_a. Considering the position x_a will usually not be an integer multiple of Δx and $x_j = j\Delta x$, we first determine the cell I_{j+k}, $k = \left[\frac{x_a - (x_j - 0.5\Delta x)}{\Delta x}\right]$, in which x_a is located. Here $[\cdot]$ is the floor function. Then, we choose a piecewise quadratic interpolation using the reconstructed values at the cell interfaces and

the point value at x_{j+k} given by Eq. (49) to compute the anticipated variables. As an example, $(\rho_a)_j$ is computed by

$$(\rho_a)_j = \rho_{j+k} + \left[\rho^-_{j+k+\frac{1}{2}} - \rho^+_{j+k-\frac{1}{2}}\right]\left(\frac{x_a - x_{j+k}}{\Delta x}\right) + 2\left[\rho^-_{j+k+\frac{1}{2}} - 2\rho_{j+k} + \rho^+_{j+k-\frac{1}{2}}\right]\left(\frac{x_a - x_{j+k}}{\Delta x}\right)^2. \quad (64)$$

This procedure is an extension of the idea in [17,32]. For non-periodic boundary conditions, if x_a is beyond the right boundary, we compute the anticipated variables based on the specification of boundary conditions suggested by Helbing and Treiber [62].

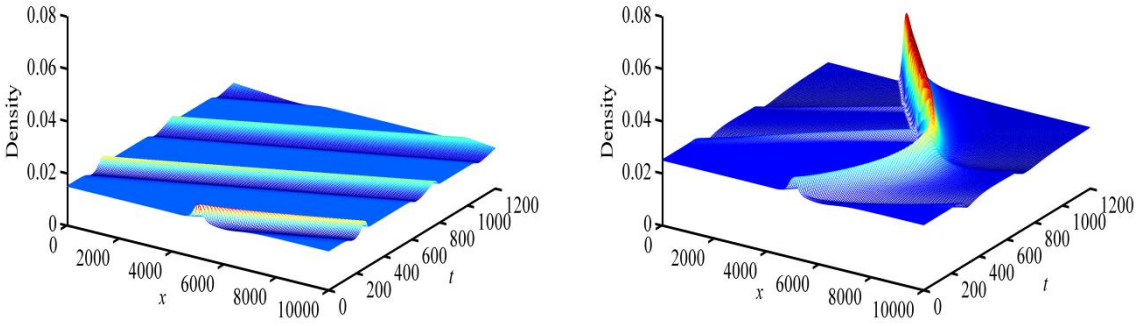

(a) (b)

Fig. 27. GKT model, the evolution of the density computed by the CU-MP5 scheme. (a) $\bar{\rho} = 0.015$; (b) $\bar{\rho} = 0.025$.

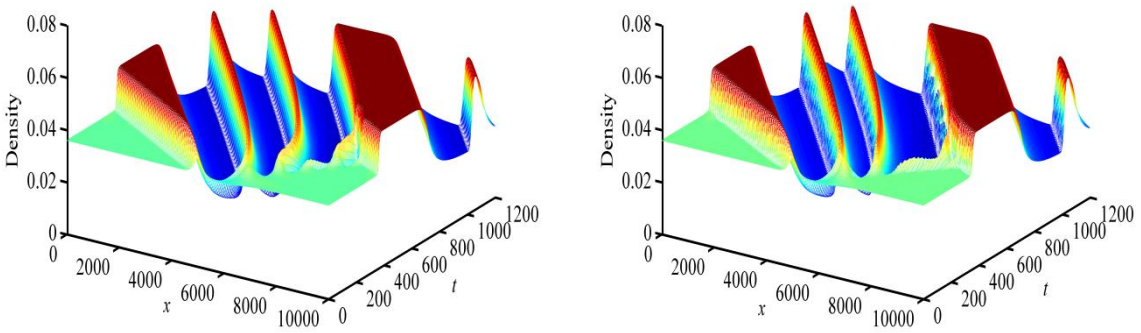

(a) (b)

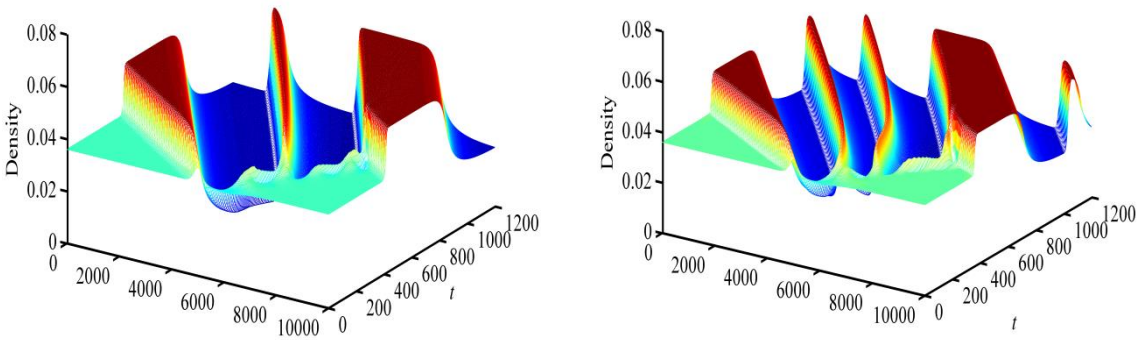

(c) (d)

Fig. 28. GKT model, the evolution of the density for $\bar{\rho} = 0.036$. (a) CU-MP5 scheme with 400 points; (b) CU-MP5 scheme with 800 points; (c) CU1 scheme with 400 points; (d) CU1 scheme with 1600 points.

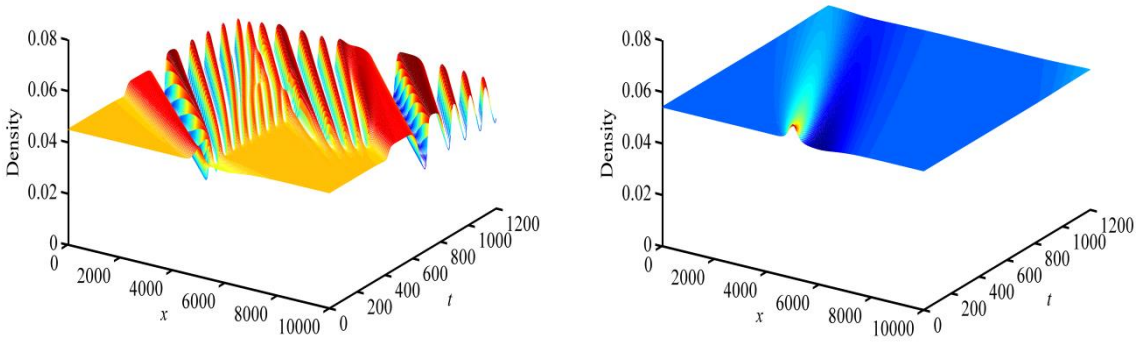

(a) (b)

Fig. 29. GKT model, the evolution of the density computed by the CU-MP5 scheme. (a) $\bar{\rho} = 0.045$; (b) $\bar{\rho} = 0.054$.

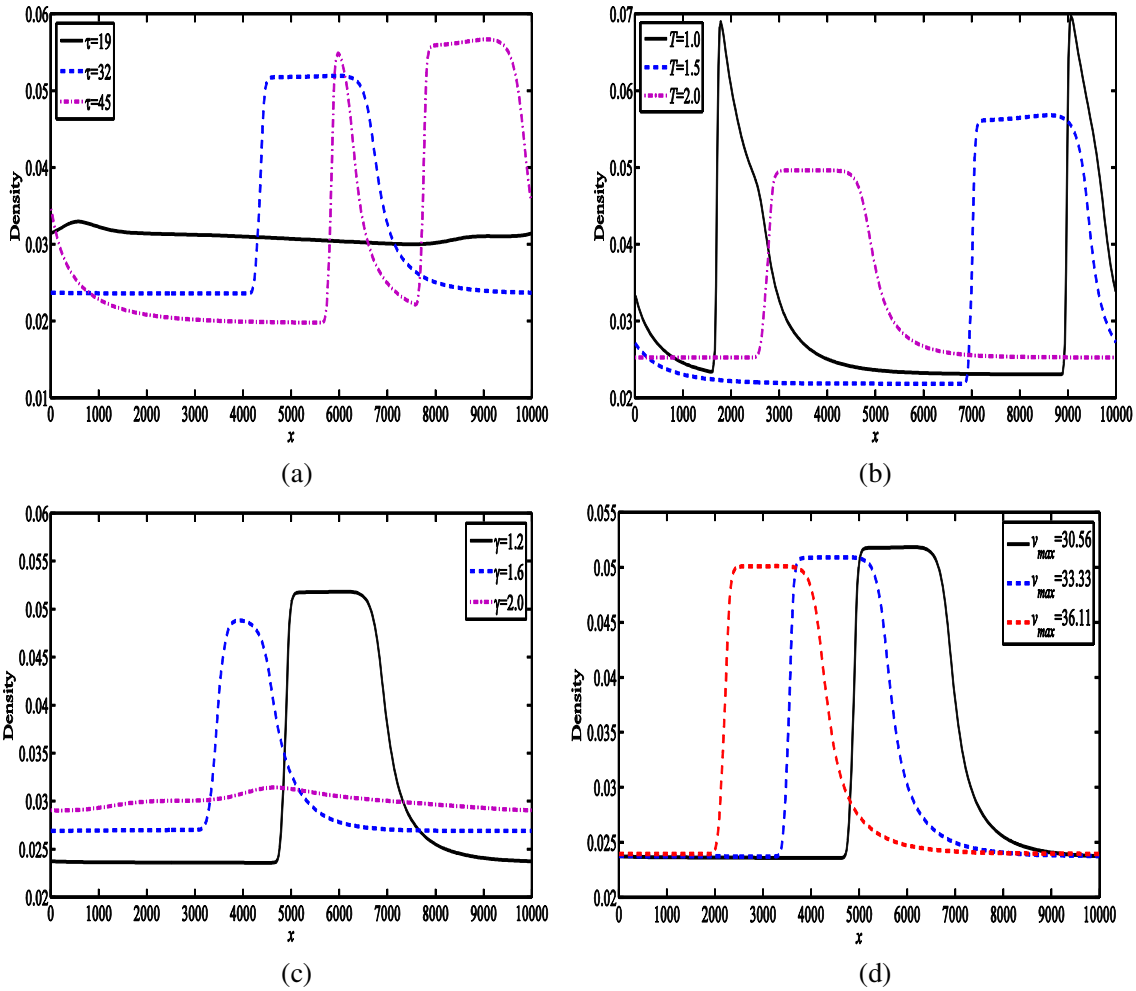

(a) (b)

(c) (d)

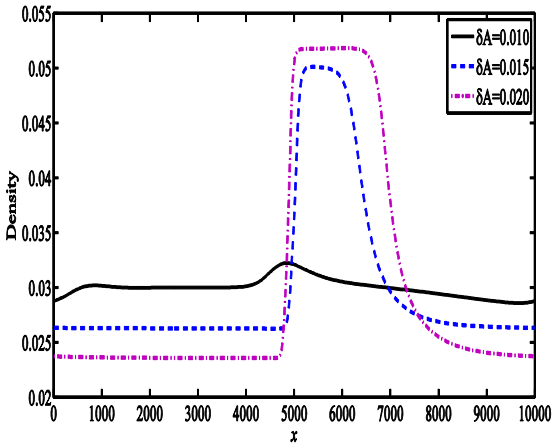

(e)

Fig. 30. GKT model, the density computed by the CU-MP5 scheme. The variation of the model parameters (a) the relaxation time τ ($\bar{\rho}=0.031$ veh/m); (b) the safe time headway T ($\bar{\rho}=0.031$ veh/m); (c) the anticipation factor γ ($\bar{\rho}=0.03$ veh/m); (d) the desired velocity $v_{\max}$ ($\bar{\rho}=0.03$ veh/m); (e) δA ($\bar{\rho}=0.03$ veh/m).

5. Conclusions

In this paper, high-resolution central-upwind approximation has been introduced and investigated to obtain numerical solutions of traffic flow models. A unified numerical discretization framework that can be applicable for different second-order models have been presented. The resulting method is simple and free of Riemann solvers and characteristic decomposition. Moreover, due to high-order reconstructions for spatial discretization, the method has higher accuracy. Numerical results show the superiority of higher-order discretization over the first-order one. They reduce the excessive numerical dissipation and produce sharper resolution. Furthermore, high-order methods need fewer grid points to achieve the desired accuracy and resolution and to resolve the problems in which solutions contain rich region structures. Thus, considering the performance on different second-order macroscopic traffic flow models, the CU scheme appears to be a very promising numerical method for traffic flow models and can be considered to apply to some new models and to real traffic simulations.

Acknowledgments

This work was supported by the National Natural Science Foundation of China (No. 11772264). The first author would like to acknowledge the China Scholarship Council for sponsoring his visit to the University of Leeds.

Reference

[1] M.D. Rosini, Macroscopic models for vehicular flows and crowd dynamics: theory and applications, Springer, 2013.

[2] M.J. Lighthill, G.B. Whitham, On kinematic waves. II. A theory of traffic flow on long crowded roads, Proc. R. Soc. Lond. A 229 (1955) 317–345.

[3] P.I. Richards, Shock waves on the highway, Oper. Res. 4 (1956) 42–51.

[4] H.M. Zhang, R. Kuhne, P. Michalopoulos, Continuum flow models, in: N.H. Gartner, C.J. Messer, A. Rathi (Eds.), Traffic flow theory: a state-of-the-art report, Transportation Research Board, Washington, DC, 2001, (Chapter 5).

[5] H.J. Payne, Model of freeway traffic and control, Mathematical Models of Public Systems 28 (1971) 51–61.

[6] G.B.Whitham, Linear and nonlinear waves, John Wiley and Sons, New York, 1974.

[7] H.M. Zhang, A theory of nonequilibrium traffic flow, Transp. Res. Part B 32 (1998) 485–498.

[8] A. Aw, M. Rascle, Resurrection of second order models of traffic flow, SIAM J. Appl. Math. 60 (2000) 916–938.

[9] H.M. Zhang, A non-equilibrium traffic model devoid of gas-like behavior, Transp. Res. Part B 36 (2002) 275–290.

[10] P. Zhang, S.C. Wong, C.W. Shu, A weighted essentially non-oscillatory numerical scheme for a multi-class traffic flow model on an inhomogeneous highway, J. Comput. Phys. 212 (2006) 739–756.

[11] S.K. Godunov, A difference method for numerical calculation of discontinuous solutions of the equations of hydrodynamics, Mat. Sb. 47 (1959) 271–306.

[12] J.P. Lebacque, The Godunov scheme and what it means for first order traffic flow models. In: Proceedings of the 13th International Symposium on Transportation and Traffic Theory, 1996, pp. 647–678.

[13] C.F. Daganzo, The cell transmission model: A dynamic representation of highway traffic consistent with the hydrodynamic theory, Transp. Res. Part B 28 (1994) 269–287.

[14] C.F. Daganzo, The cell transmission model, part II: network traffic, Transp. Res. Part B 29 (1995) 79–93.

[15] C.F. Daganzo, Requiem for second-order fluid approximations to traffic flow, Transp. Res. Part B 29 (1995) 277–286.

[16] M. Treiber, A. Hennecke, D. Helbing, Derivation, properties, and simulation of a gas-kinetic-based, nonlocal traffic model, Phys. Rev. E 59 (1999) 239–253.

[17] M. Treiber, A. Kesting, Traffic flow dynamics: data, models and simulation, Springer-Verlag Berlin Heidelberg, 2013.

[18] G.C.K. Wong, S.C. Wong, A multi-class traffic flow model-an extension of LWR model with heterogeneous drivers, Transp. Res. Part A 36 (2002) 827–841.

[19] H.M. Zhang, A finite difference approximation of a non-equilibrium traffic flow model, Transp. Res. Part B 35 (2001) 337–365.

[20] J.V. Morgan, Numerical methods for macroscopic traffic models, Ph.D. thesis, University of Reading, 2002.

[21] W.L. Jin, H.M. Zhang, The formation and structure of vehicle clusters in the Payne-Whitham traffic flow model, Transp. Res. Part B 37 (2003) 207–223.

[22] W.L. Jin, Traffic flow models and their numerical solutions, Master thesis, University of California, Davis, 2000.

[23] C. Niyitegeka, Numerical comparisons of traffic flow models, Master thesis, TU-Kaiserlautern and TU-Eindhoven, 2012.

[24] M. Zhang, C.W. Shu, G.C.K. Wong, S.C. Wong, A weighted essentially non-oscillatory numerical scheme for a multi-class Lighthill-Whitham-Richards traffic flow model, J. Comput. Phys. 191 (2003) 639–659.

[25] G.S. Jiang, C.W. Shu, Efficient implementation of weighted ENO schemes, J. Comput. Phys. 126 (1995) 202–228.

[26] J.K. Wiens, J.M. Stockie, J. Williams, Riemann solver for a kinematic wave traffic model with discontinuous flux, J. Comput. Phys. 242 (2011) 1–23.

[27] M. Garavello, P. Goatin, The Aw-Rascle traffic model with locally constrained flow, J. Math. Anal. Appl. 378 (2011) 634–648.

[28] D. Ngoduy, Instability of cooperative adaptive cruise control traffic flow: A macroscopic approach, Commun. Nonlinear Sci. Numer. Simul. 18 (2013) 2838–2851.

[29] A.I. Delis, I.K. Nikolos, M. Papageorgiou, Macroscopic traffic flow modeling with adaptive cruise control: Development and numerical solution, Comput. Math. Appl. 70 (2015) 1921–1947.

[30] J.Z. Chen, Z.K. Shi, Y.M. Hu, A relaxation scheme for a multi-class Lighthill-Whitham-Richards traffic flow model, J. Zhejiang Univ.- SCI. A 10 (2009) 1835–1844.

[31] J.Z. Chen, Z.K. Shi, Y.M. Hu, Numerical solutions of a multiclass traffic flow model on an inhomogeneous highway using a high-resolution relaxed scheme, J. Zhejiang Univ.-SCI. C 13 (2012) 29–36.

[32] A.I. Delis, I.K. Nikolos, M. Papageorgiou, High-resolution numerical relaxation approximations to second-order macroscopic traffic flow models, Transp. Res. Part C 44 (2014) 318–349.

[33] A. Kurganov, S. Noelle, G. Petrova, Semidiscrete central-upwind schemes for hyperbolic conservation laws and Hamilton–Jacobi equations, SIAM J. Sci. Comput. 23 (2001) 707–740.

[34] A. Beljadid, A. Mohammadian, A. Kurganov, Well-balanced positivity preserving cell-vertex central-upwind scheme for shallow water flows, Computers & Fluids, 136 (2016) 193–206.

[35] S. Khorshid, A. Mohammadian, I. Nistor, Extension of a well-balanced central upwind scheme for variable density shallow water flow equations on triangular grids, Computers & Fluids, 156 (2017) 441–448.

[36] X. Liu, J. Albright, Y. Epshteyn, A. Kurganov, Well-balanced positivity preserving central-upwind scheme with a novel wet/dry reconstruction on triangular grids for the Saint-Venant system, J. Comput. Phys. 374 (2018) 213–236.

[37] B.M. Ginting, Central-upwind scheme for 2D turbulent shallow flows using high-resolution meshes with scalable wall functions. Computers & Fluids, 179 (2019) 394–421.

[38] J.Z. Chen, Z.K. Shi, Y.M. Hu, Numerical solution of a two-class LWR traffic flow model by high-resolution central-upwind scheme, Computational Science–ICCS 2007, Springer, 2007, pp.17–24.

[39] Y.M. Hu, J.H. Feng, J.Z. Chen, A semi-discrete central-upwind scheme for a multi-class Lighthill-Whitham-Richards traffic flow model, Chinese J. Comput. Phys. 31 (2014) 323–330.

[40] A. Kurganov, A. Polizzi, Non-oscillatory central schemes for traffic flow models with Arrhenius look-ahead dynamics, Netw. Heterog. Media 4 (2009) 431–451.

[41] H. Nessyahu, E. Tadmor, Non-oscillatory central differencing for hyperbolic conservation laws, J. Comput. Phys. 87 (1990) 408–463.

[42] S. Blandin, P. Goatin, Well-posedness of a conservation law with non-local flux arising in traffic flow modeling, Numer. Math. 132 (2016) 217–241.

[43] R.D. Kuhne, Freeway speed distribution and acceleration noise: calculations from a stochastic continuum theory and comparison with measurements, The Proceedings of the Tenth International Symposium on Transportation and Traffic Theory, 1987, pp. 119–137.

[44] B.S. Kerner, P. Konhäuser, Cluster effect in initially homogeneous traffic flow, Phys. Rev. E 48 (1993) R2335–R2338.

[45] J.M. Del Castillo, P. Pintado, F.G. Benitez, The reaction time of drivers and the stability of traffic flow, Transp. Res. Part B 28 (1994) 35–60.

[46] B.S. Kerner, P. Konhäuser, Structure and parameters of clusters in traffic flow, Phys. Rev. E 50 (1994) 54–83.

[47] M. Hermann, B.S. Kerner, Local cluster effects in different traffic flow models, Physica A 255 (1998) 163–198.

[48] H.M. Zhang, Structural properties of solutions arising from a nonequilibrium traffic flow theory, Transp. Res. Part B 34 (2000) 583–603.

[49] W.L. Jin, H.M. Zhang, Solving the Payne–Whitham traffic flow model as a hyperbolic system of conservation laws with relaxation, Technical Report, University of California, Davis, 2001.

[50] J.M. Greenberg, Extensions and amplifications of a traffic model of Aw and Rascle, SIAM J. Appl. Math. 62 (2001) 729–745.

[51] R. Jiang, Q.S. Wu, Z.J. Zhu, A new continuum model for traffic flow and numerical tests, Transp. Res. Part B 36 (2002) 405–419.

[52] Y. Xue, S.Q. Dai, Continuum traffic model with the consideration of two delay time scales, Phys. Rev. E 68 (2003) 66123.

[53] P. Zhang, S.C. Wong, S.Q. Dai, A conserved higher-order anisotropic traffic flow model: description of equilibrium and non-equilibrium flows, Transp. Res. Part B 43 (2009) 562–574.

[54] J.Z. Chen, Z.K. Shi, Y.M. Hu, L. Yu, Y. Fang, An extended macroscopic model for traffic flow on a highway with slopes, Int. J. Mod. Phys. C 24 (2013) 1350061.

[55] S. Mammar, J.P. Lebacque, H.H. Salem, Riemann problem resolution and Godunov scheme for the Aw-Rascle-Zhang model, Transport. Sci. 43 (2009) 531–545.

[56] D. Helbing, A. Hennecke, V. Shvetsov, M. Treiber, MASTER: Macroscopic traffic simulation based on a gas-kinetic, non-local traffic model, Transp. Res. Part B 35 (2001) 183–211.

[57] H.M. Zhang, Driver memory, traffic viscosity and a viscous vehicular traffic flow model, Transp. Res. Part B 37 (2003) 27–41.

[58] R. Borges, M. Carmona, B. Costa, W.S. Don, An improved weighted essentially non-oscillatory scheme for hyperbolic conservation laws, J. Comput. Phys. 227 (2008) 3191–3211.

[59] A. Suresh, H. Huynth, Accurate monotonicity-preserving schemes with Runge-Kutta time stepping, J. Comput. Phys. 136 (1997) 83–99.

[60] S. Gottlieb, C.W. Shu, E. Tadmor, Strong stability-preserving high-order time discretization methods, SIAM Rev. 43 (2001) 89–112.

[61] J. Shi, C. Hu, C.W. Shu, A technique of treating negative weights in WENO schemes, J. Comput. Phys. 175 (2002) 108–127.

[62] D. Helbing, M. Treiber, Numerical simulation of macroscopic traffic equations, Comput. Sci. Eng. 1 (1999) 89–98.